PHYSICAL REVIEW D VOLUME 44, NUMBER 7 1 OCTOBER 1991

ARTICLES

Higher-twist effects in the reaction $\pi^- N \rightarrow \mu^+\mu^- X$ at 253 GeV/c

J. G. Heinrich, C. Biino,* J. F. Greenhalgh,† W. C. Louis,‡ K. T. McDonald, S. Palestini,* D. P. Russell, F. C. Shoemaker, and A. J. S. Smith
Joseph Henry Laboratories, Princeton University, Princeton, New Jersey 08544

C. E. Adolphsen,§ J. P. Alexander,** K. J. Anderson, J. S. Conway,†† J. E. Pilcher, and A. Possoz‡‡
Enrico Fermi Institute, University of Chicago, Chicago, Illinois 60637

E. I. Rosenberg
Ames Laboratory, Iowa State University, Ames, Iowa 50011
(Received 1 April 1991)

The distributions of quarks in the pion and nucleon are extracted from measurements of the reaction $\pi^- N \rightarrow \mu^+\mu^- X$ at 253 GeV/c in a naive Drell-Yan analysis, as well as QCD-corrected analyses at leading-log and next-to-leading-log order. As $x_\pi \rightarrow 1$ the pion structure function shows a term that varies as $1/m_{\mu\mu}^4$, which we interpret as a higher-twist effect. Additionally, the angular distribution of the μ^+ in the muon-pair rest frame tends towards $\sin^2\theta$ as $x_\pi \rightarrow 1$ and as $m_{\mu\mu} \rightarrow 0$ in a manner consistent with higher-twist effects. When the strongly mass-dependent higher-twist effects are included as part of the pion structure function, the nucleon structure function agrees well with leading-twist results from deeply inelastic lepton-hadron scattering. A significant advance of the present work is the extension of the analysis to low masses by the subtraction of the J/ψ and ψ' resonances from the continuum. Our analysis covers the kinematic range $0.4 < x_\pi < 1.0$ and $0.02 < x_N < 0.33$ with $3.0 < m_{\mu\mu} < 8.55$ GeV/c^2. Cross sections for ψ' production are presented in an appendix.

I. INTRODUCTION

In 1968 Christenson *et al.* [1] discovered a continuum of massive muon pairs produced in hadron collisions. Subsequently, Drell and Yan [2] nominated parton-antiparton annihilation as a possible explanation. At lowest order in the Drell-Yan model (the "naive" analysis) a quark and an antiquark from the incident hadrons annihilate; the resulting massive virtual photon then decays into a pair of leptons. Higher-order QCD corrections add one or more gluons to the lowest-order diagram; these corrections substantially increase the lepton-pair-production cross section [3, 4]. Another class of corrections includes the effects of the strong forces that bind the constituent partons of the incident hadrons [5]. The term "higher twist" [6] is applied to these interactions that involve more than the minimum number of constituent partons.

In association with our initial measurement of the pion structure function [7] by analysis of the reaction $\pi^- N \rightarrow \mu^+\mu^- X$, we found that the decay angular distribution of the μ^+ in the μ-pair rest frame changes as x_π approaches 1 [8]. This effect was interpreted as evidence for higher-twist corrections, and was confirmed in our subsequent experiments [9, 10]. However, we found in Ref. [10] that the μ-pair production cross section at large x_π and low $m_{\mu\mu}$ showed an excess above that accommodated in a leading-log Drell-Yan analysis that included a higher-twist correction varying as $1/m_{\mu\mu}^2$. This work considered the mass region $m_{\mu\mu} > 4.05$ GeV/c^2, chosen to eliminate any contribution from the J/ψ and ψ' resonances. The cross-section excess appeared to fall rapidly with increasing mass. In the present work we extend the cross-section analysis to include the 3–4 GeV/c^2 mass region by a careful subtraction of the resonance contribution. We also extend the Drell-Yan analysis of the cross section to include a broader class of QCD corrections.

To distinguish higher-twist effects from lowest-twist QCD corrections, the data will be compared to cross sections calculated to leading-log and next-to-leading-log order (in addition to the lowest order). Leading-log order includes the evolution of the quark distributions. This evolution, well established in deeply inelastic lepton scattering, is governed by the Altarelli-Parisi equations of QCD [11]. Appendix C contains a summary of the method used to implement the leading-log approximation.

 ©1991 The American Physical Society

The next-to-leading-log approximation [3, 4] includes the evolution of the leading-log scheme and also the complete first-order term in the QCD perturbation series (expressed in powers of the strong-interaction coupling constant α_S). The main consequence of this is to increase the cross section by a factor of ~ 1.7, approximately constant over the region of phase space covered by this experiment. A summary of the procedure used to implement the next-to-leading-log approximation appears in Appendix D.

Among our previous studies of higher-twist effects, Refs. [8] and [9] made no attempt to include the lowest-twist QCD corrections, while Ref. [10] included the leading-log corrections. We find below that the qualitative effect of the next-to-leading-order QCD corrections on the interpretation of our data is very slight, other than the overall increase in the model cross sections mentioned above. This is largely because our muon-pair mass range of 3 to 9 GeV/c^2 is not sufficient to reveal logarithmic effects. The higher-twist effects, however, are quite noticeable as they vary as an inverse power of the mass.

This paper begins with brief discussions of the kinematical definitions used later (Sec. II), of the apparatus (Sec. III), and of the event analysis (Sec. IV). The resonance subtraction procedure is presented in Sec. V, and some consequent results on ψ' production are given in Appendix F. The main results on the pion and nucleon structure functions are given in Sec. VI, which includes subsections on the naive analysis, QCD-corrected analyses, higher-twist effects, and also a reanalysis of our 80-GeV/c data [9] which lends support to the new interpretation of our 253-GeV/c data. Section VII discusses how observed variations in the angular distribution of the μ^+ are consistent with the higher-twist effects found in Sec. VI. Some conclusions are presented in Sec. VIII.

II. KINEMATICS

The kinematics of a muon pair can be characterized by 6 variables: the invariant mass $m_{\mu\mu}$, the Feynman x, the transverse momentum p_T, the laboratory azimuthal angle $\phi_{\rm lab}$, and the angles θ and ϕ of the μ^+ with respect to the beam direction in the muon-pair rest frame. The results in this paper have been averaged over p_T, $\phi_{\rm lab}$, and ϕ. The dependence of our muon-pair data sample on p_T and ϕ was discussed in Ref. [10]; some additional remarks on the p_T dependence are given at the end of Sec. IV below.

The longitudinal-momentum fraction x_F is defined here as

$$x_F = \frac{2p_L}{\sqrt{s}},$$

where p_L is the component of the $\mu^+\mu^-$ pair momentum parallel to the direction of the incident pion beam (in the center-of-mass frame of the initial hadrons), and s is the square of the energy of the initial-state particles. The momentum fractions x_π and x_N are then defined by the two equations

$$x_F = x_\pi - x_N, \qquad m_{\mu\mu}^2 = x_\pi x_N s,$$

where $m_{\mu\mu}$ is the mass of the $\mu^+\mu^-$ pair.

The definition of x_π given above is standard in the literature but has the unfortunate artifact that the momentum fraction of the antiquark in the pion depends on the nucleon mass. Reference [12] discusses definitions that are closer to the spirit of the QCD calculations. However, to facilitate comparison with previously reported results we continue to use the usual definitions.

In this study we have only used data with x_π greater than 0.4. This cut was selected to eliminate any significant influence by pion sea quarks, since the pion sea-quark distribution is small compared with the valence-quark distribution for $x_\pi > 0.4$ [13]. This simplified the calculation of the cross section, and reduced systematic errors associated with uncertainties in the pion sea and in corrections for secondary interactions in the target. Our previously published analysis [10] with $m_{\mu\mu} > 4.05$ GeV/c^2 did include the data with $x_\pi > 0.2$, $x_F > 0.0$.

III. EXPERIMENTAL APPARATUS

The experimental apparatus has been described in detail in Refs. [10] and [14]. It was a two-magnet spectrometer that triggered on muon pairs. These pairs were produced in a tungsten target by 253-GeV/c π^- in the Fermilab Proton-West beam line. The beam intensity was 4×10^9 pions per 20-sec spill. Hadrons produced in the target were attenuated by beryllium and carbon absorbers located in the gap of the first magnet. High-mass muon pairs were focused by this magnet into the analyzing spectrometer consisting of a second magnet surrounded by 25 planes of proportional and drift chambers for particle tracking and 8 scintillator planes for triggering. The trigger selected muon pairs with an estimated mass above 2.0 GeV/c^2. The apparatus was designed to have a large acceptance for muon pairs with a high x_F.

IV. EVENT ANALYSIS

The reconstruction and selection of events and the Monte Carlo simulation of the experiment largely followed Ref. [10]; only significant differences will be mentioned here. The data sample consisted of events with $x_\pi > 0.4$ and 2.0 GeV/c^2 $< m_{\mu\mu} <$ 8.5 GeV/c^2, the upper limit on $m_{\mu\mu}$ being set by the Υ resonances.

A significant background due to beam-associated muons was largely eliminated by requiring $-0.75 < \cos\theta < 0.85$, where θ is defined by the direction of the μ^+ relative to the beam direction in the $\mu^+\mu^-$ pair rest frame. As we used a negative beam the background is most prominent at $\cos\theta = -1$ and large x_F. This background might be wrongly interpreted as novel physics at large x, so it is important that it be minimized. The magnitude of the background that survives the $\cos\theta$ cut can be judged from Fig. 12 in Sec. VII below. Our previous analysis [10] used a model of this background to allow a slightly larger range in $\cos\theta$.

The acceptance of the experiment was calculated using a Monte Carlo simulation that generated $\mu^+\mu^-$ pairs

according to our measured differential cross sections and beam-momentum spectrum. Since measurement of the differential cross sections requires knowledge of the experimental acceptance, the final Monte Carlo generation spectra were the result of several iterations of the analysis. Contrary to our previous analysis, no attempt was made to remove Fermi-motion effects from the shape of the nucleon parton distributions: any nucleon quark distributions reported here include the influence of Fermi motion as well as any other nuclear effects. This is consistent with the current convention in deeply inelastic lepton scattering.

The calculated acceptances and associated statistical uncertainties are reported for bins of x_π-x_N in Table I.

Although our measurement of $d\sigma/dp_T$ is not emphasized in this paper, it plays an important role in the Monte Carlo simulation of the experiment. Because the detector acceptance decreases somewhat as p_T increases, the Monte Carlo program must use the proper p_T spectrum to ensure the calculation of reliable acceptances. Our previous analysis [10] gives detailed parametrizations of the $m_{\mu\mu}$ and x_F dependence of the p_T spectrum for the $m_{\mu\mu} > 4.0\ \mathrm{GeV}/c^2$ portion of this data set; these spectra are used in both the current Monte Carlo program and the Monte Carlo program of the previous analysis to generate events in that mass range. We have extended the p_T analysis for the $m_{\mu\mu} < 4.0\ \mathrm{GeV}/c^2$ portion of the data set. The p_T spectra resulting from this additional analysis are used to generate Monte Carlo events in the lower-mass range. The p_T spectra of Ref. [10] show a significant decrease in $\langle p_T \rangle$ at low mass and at high x_F; this trend continues in the lower-mass range of the extended analysis.

TABLE I. Measured cross section in bins of x_π and x_N (a global 15% uncertainty also applies). Also given are the higher-twist fraction (F_{HT}, the fraction of the cross section due to higher-twist effects), the acceptance, and the continuum fraction (F_c, the fraction of raw data due to the continuum).

x_π		x_N		$d^2\sigma/dx_\pi\,dx_N$	F_{HT}	Acceptance	F_c
Low	High	Low	High	(nb/nucleon)	(%)	(%)	(%)
0.58	0.60	0.02	0.03	34.7±1.3	12±3	15.1±0.4	36.7±0.8
0.60	0.62	0.02	0.03	34.8±1.7	13±3	15.1±0.5	30.2±1.1
0.62	0.64	0.02	0.03	26.6±1.3	14±3	16.1±0.5	21.0±0.8
0.64	0.66	0.02	0.03	24.4±1.0	15±3	15.9±0.5	17.3±0.5
0.66	0.68	0.02	0.03	21.74±0.95	16±3	16.7±0.5	15.1±0.4
0.68	0.70	0.02	0.03	17.7±1.5	17±3	17.3±0.6	12.8±1.0
0.70	0.72	0.02	0.03	17.39±0.86	18±3	16.8±0.6	12.9±0.4
0.72	0.74	0.02	0.03	15.55±0.87	19±2	16.8±0.6	12.6±0.5
0.74	0.76	0.02	0.03	14.76±0.67	21±2	16.6±0.6	13.7±0.3
0.76	0.78	0.02	0.03	14.3±1.1	22±2	17.0±0.7	16.0±1.0
0.78	0.80	0.02	0.03	11.54±0.56	24±2	18.3±0.7	16.9±0.5
0.80	0.82	0.02	0.03	11.94±0.62	25±2	17.1±0.7	19.9±0.5
0.82	0.84	0.02	0.03	11.05±0.63	27±2	16.7±0.8	23.0±0.7
0.84	0.86	0.02	0.03	9.28±0.55	30±2	17.5±0.8	25.8±0.9
0.86	0.88	0.02	0.03	8.55±0.54	33±2	17.8±0.9	30.9±1.1
0.88	0.90	0.02	0.03	6.99±0.44	37±2	18.7±1.0	36.7±1.2
0.90	0.92	0.02	0.03	5.52±0.39	43±3	20.0±1.1	42.1±1.6
0.92	0.94	0.02	0.03	4.34±0.34	51±3	21.8±1.2	57.5±2.6
0.94	0.96	0.02	0.03	3.56±0.47	63±4	17.8±1.2	55.7±6.0
0.96	0.98	0.02	0.03	2.63±0.40	78±4	20.2±1.6	75.1±9.1
0.98	1.00	0.02	0.03	1.67±0.21	95±3	17.7±1.7	84.6±3.8
0.58	0.60	0.03	0.04	14.97±0.78	6±2	17.5±0.6	5.2±0.2
0.60	0.62	0.03	0.04	14.71±0.79	7±2	17.7±0.6	6.1±0.2
0.62	0.64	0.03	0.04	11.81±0.66	7±2	17.8±0.7	6.0±0.2
0.64	0.66	0.03	0.04	10.03±0.47	8±2	19.6±0.7	7.3±0.2
0.66	0.68	0.03	0.04	9.48±0.47	9±2	18.3±0.7	8.8±0.2
0.68	0.70	0.03	0.04	7.78±0.52	9±2	20.3±0.8	11.0±0.6
0.70	0.72	0.03	0.04	7.39±0.40	10±2	19.6±0.8	15.0±0.5
0.72	0.74	0.03	0.04	6.24±0.52	11±2	20.5±0.9	19.0±1.3
0.74	0.76	0.03	0.04	5.31±0.32	12±2	23.3±1.0	27.2±1.0
0.76	0.78	0.03	0.04	5.16±0.35	13±2	22.7±1.1	36.9±1.7
0.78	0.80	0.03	0.04	4.79±0.35	14±2	21.6±1.1	45.8±2.2
0.80	0.82	0.03	0.04	4.68±0.35	15±2	21.4±1.1	56.6±2.6
0.82	0.84	0.03	0.04	4.22±0.37	16±2	21.3±1.2	65.7±4.1
0.84	0.86	0.03	0.04	3.18±0.38	18±2	22.0±1.3	64.1±6.4
0.86	0.88	0.03	0.04	3.16±0.29	20±3	20.9±1.3	81.5±4.5

TABLE I. (*Continued*).

x_π Low	x_π High	x_N Low	x_N High	$d^2\sigma/dx_\pi\,dx_N$ (nb/nucleon)	F_{HT} (%)	Acceptance (%)	F_c (%)
0.88	0.90	0.03	0.04	2.27±0.24	24±3	23.1±1.5	85.5±5.9
0.90	0.92	0.03	0.04	2.25±0.22	28±4	20.3±1.5	91.7±3.6
0.92	0.94	0.03	0.04	1.90±0.20	36±5	20.1±1.6	94.9±3.5
0.94	0.96	0.03	0.04	1.08±0.24	48±6	21.4±2.0	77.1±14.4
0.96	0.98	0.03	0.04	0.79±0.11	66±8	20.3±2.2	99.7±2.5
0.98	1.00	0.03	0.04	0.470±0.081	91±5	21.5±2.8	97.2±2.4
0.58	0.60	0.04	0.05	8.33±0.52	4±1	15.2±0.7	23.2±1.0
0.60	0.62	0.04	0.05	8.20±0.55	4±1	15.6±0.7	34.0±1.6
0.62	0.64	0.04	0.05	6.76±0.41	5±1	16.4±0.7	37.7±1.3
0.64	0.66	0.04	0.05	6.54±0.43	5±2	15.6±0.8	44.8±1.6
0.66	0.68	0.04	0.05	5.49±0.38	5±2	16.6±0.9	48.1±1.8
0.68	0.70	0.04	0.05	5.30±0.40	6±2	16.8±0.9	55.7±2.5
0.70	0.72	0.04	0.05	4.06±0.33	6±2	19.3±1.0	62.1±3.3
0.72	0.74	0.04	0.05	3.61±0.39	7±2	19.2±1.1	68.3±5.8
0.74	0.76	0.04	0.05	3.78±0.32	7±2	18.7±1.1	81.9±3.6
0.76	0.78	0.04	0.05	3.16±0.25	8±2	19.6±1.2	90.8±2.5
0.78	0.80	0.04	0.05	2.46±0.20	9±2	20.6±1.3	93.7±2.1
0.80	0.82	0.04	0.05	2.64±0.23	10±2	19.5±1.3	98.8±1.8
0.82	0.84	0.04	0.05	2.04±0.18	11±2	21.0±1.5	98.8±0.6
0.84	0.86	0.04	0.05	1.78±0.17	12±2	21.2±1.6	99.7±0.4
0.86	0.88	0.04	0.05	1.45±0.14	14±3	22.8±1.7	100.0±0.1
0.88	0.90	0.04	0.05	1.12±0.12	16±3	24.2±1.9	100.0±0.0
0.90	0.92	0.04	0.05	0.99±0.12	20±4	21.0±1.8	100.0±0.0
0.92	0.94	0.04	0.05	0.86±0.11	26±5	20.0±2.0	100.0±0.0
0.94	0.96	0.04	0.05	0.561±0.082	36±7	23.2±2.5	100.0±0.0
0.96	0.98	0.04	0.05	0.311±0.055	56±10	25.4±3.2	100.0±0.0
0.98	1.00	0.04	0.05	0.234±0.051	87±8	25.1±4.1	100.0±0.0
0.58	0.60	0.05	0.06	5.47±0.67	3±1	12.0±0.7	59.9±6.2
0.60	0.62	0.05	0.06	5.67±0.78	3±1	13.0±0.7	88.0±10.5
0.62	0.64	0.05	0.06	3.98±0.35	3±1	14.4±0.8	84.6±4.3
0.64	0.66	0.05	0.06	3.91±0.32	3±1	15.7±0.9	96.8±3.4
0.66	0.68	0.05	0.06	3.51±0.30	4±1	14.8±0.9	95.0±2.9
0.68	0.70	0.05	0.06	3.42±0.29	4±1	15.2±1.0	99.7±0.6
0.70	0.72	0.05	0.06	2.41±0.21	4±1	16.4±1.1	99.9±0.2
0.72	0.74	0.05	0.06	2.43±0.22	5±1	16.0±1.1	99.9±0.1
0.74	0.76	0.05	0.06	2.23±0.21	5±2	16.3±1.2	100.0±0.0
0.76	0.78	0.05	0.06	1.71±0.17	6±2	17.4±1.4	100.0±0.0
0.78	0.80	0.05	0.06	1.79±0.19	6±2	16.3±1.3	100.0±0.0
0.80	0.82	0.05	0.06	1.38±0.15	7±2	18.5±1.6	100.0±0.0
0.82	0.84	0.05	0.06	1.15±0.13	7±2	20.4±1.7	100.0±0.0
0.84	0.86	0.05	0.06	0.90±0.11	8±2	19.3±1.8	100.0±0.0
0.86	0.88	0.05	0.06	1.02±0.14	10±2	16.7±1.8	100.0±0.0
0.88	0.90	0.05	0.06	0.85±0.12	11±3	17.2±1.8	100.0±0.0
0.90	0.92	0.05	0.06	0.558±0.085	14±4	19.5±2.1	100.0±0.0
0.92	0.94	0.05	0.06	0.331±0.056	19±5	24.2±2.8	100.0±0.0
0.94	0.96	0.05	0.06	0.226±0.050	28±7	18.3±2.5	100.0±0.0
0.96	0.98	0.05	0.06	0.221±0.049	46±12	23.2±3.7	100.0±0.0
0.98	1.00	0.05	0.06	0.103±0.032	83±12	24.3±5.2	100.0±0.0
0.52	0.54	0.06	0.08	4.68±0.33	1±1	7.5±0.4	91.9±2.8
0.54	0.56	0.06	0.08	4.78±0.32	1±1	7.5±0.4	98.4±1.6
0.56	0.58	0.06	0.08	3.83±0.26	2±1	8.0±0.4	99.6±0.7
0.58	0.60	0.06	0.08	2.88±0.21	2±1	8.9±0.5	99.7±0.3
0.60	0.62	0.06	0.08	3.01±0.21	2±1	9.5±0.5	100.0±0.0
0.62	0.64	0.06	0.08	2.63±0.19	2±1	10.2±0.6	100.0±0.0
0.64	0.66	0.06	0.08	2.56±0.19	2±1	10.2±0.6	100.0±0.0
0.66	0.68	0.06	0.08	2.21±0.17	2±1	10.6±0.6	100.0±0.0
0.68	0.70	0.06	0.08	1.61±0.13	2±1	13.2±0.8	100.0±0.0
0.70	0.72	0.06	0.08	1.72±0.14	3±1	12.0±0.7	100.0±0.0

TABLE I. (*Continued*).

x_π		x_N		$d^2\sigma/dx_\pi\, dx_N$	F_{HT}	Acceptance	F_c
Low	High	Low	High	(nb/nucleon)	(%)	(%)	(%)
0.72	0.74	0.06	0.08	1.41±0.12	3±1	14.1±0.9	100.0±0.0
0.74	0.76	0.06	0.08	1.26±0.11	3±1	14.2±0.9	100.0±0.0
0.76	0.78	0.06	0.08	1.061±0.097	3±1	15.4±1.0	100.0±0.0
0.78	0.80	0.06	0.08	0.744±0.071	4±1	17.9±1.2	100.0±0.0
0.80	0.82	0.06	0.08	0.899±0.091	4±1	15.3±1.1	100.0±0.0
0.82	0.84	0.06	0.08	0.597±0.066	5±2	16.1±1.2	100.0±0.0
0.84	0.86	0.06	0.08	0.525±0.063	5±2	16.1±1.3	100.0±0.0
0.86	0.88	0.06	0.08	0.350±0.043	6±2	20.4±1.7	100.0±0.0
0.88	0.90	0.06	0.08	0.339±0.048	7±2	17.5±1.7	100.0±0.0
0.90	0.92	0.06	0.08	0.297±0.044	9±3	17.3±1.7	100.0±0.0
0.92	0.94	0.06	0.08	0.182±0.031	13±4	18.9±2.0	100.0±0.0
0.94	0.96	0.06	0.08	0.194±0.041	20±7	13.9±2.0	100.0±0.0
0.96	0.98	0.06	0.08	0.058±0.016	35±13	21.5±3.4	100.0±0.0
0.98	1.00	0.06	0.08	0.088±0.030	75±17	12.9±3.2	100.0±0.0
0.44	0.48	0.08	0.10	3.77±0.22	1±1	5.2±0.2	99.9±0.1
0.48	0.52	0.08	0.10	2.89±0.18	1±1	5.8±0.3	100.0±0.0
0.52	0.56	0.08	0.10	2.51±0.16	1±1	6.0±0.3	100.0±0.0
0.56	0.60	0.08	0.10	1.79±0.12	1±1	6.9±0.3	100.0±0.0
0.60	0.64	0.08	0.10	1.244±0.091	1±1	8.2±0.4	100.0±0.0
0.64	0.68	0.08	0.10	1.125±0.085	1±1	8.9±0.5	100.0±0.0
0.68	0.72	0.08	0.10	0.897±0.072	2±1	9.7±0.5	100.0±0.0
0.72	0.76	0.08	0.10	0.831±0.070	2±1	10.1±0.6	100.0±0.0
0.76	0.80	0.08	0.10	0.615±0.059	2±1	10.1±0.6	100.0±0.0
0.80	0.84	0.08	0.10	0.358±0.038	3±1	12.7±0.9	100.0±0.0
0.84	0.88	0.08	0.10	0.277±0.037	3±1	10.6±0.9	100.0±0.0
0.88	0.92	0.08	0.10	0.144±0.025	5±2	11.5±1.2	100.0±0.0
0.92	0.96	0.08	0.10	0.106±0.023	10±4	11.8±1.7	100.0±0.0
0.96	1.00	0.08	0.10	0.022±0.008	39±20	16.8±3.6	100.0±0.0
0.40	0.44	0.10	0.12	2.72±0.20	0±1	4.5±0.2	100.0±0.0
0.44	0.48	0.10	0.12	2.16±0.16	0±1	5.1±0.3	100.0±0.0
0.48	0.52	0.10	0.12	1.99±0.16	0±1	4.8±0.3	100.0±0.0
0.52	0.56	0.10	0.12	1.71±0.14	1±1	5.7±0.3	100.0±0.0
0.56	0.60	0.10	0.12	1.47±0.13	1±1	5.1±0.3	100.0±0.0
0.60	0.64	0.10	0.12	1.051±0.099	1±1	5.8±0.4	100.0±0.0
0.64	0.68	0.10	0.12	0.685±0.073	1±1	6.4±0.4	100.0±0.0
0.68	0.72	0.10	0.12	0.664±0.074	1±1	6.1±0.4	100.0±0.0
0.72	0.76	0.10	0.12	0.475±0.062	1±1	5.8±0.4	100.0±0.0
0.76	0.80	0.10	0.12	0.379±0.050	1±1	7.2±0.6	100.0±0.0
0.80	0.84	0.10	0.12	0.244±0.040	2±1	6.8±0.6	100.0±0.0
0.84	0.88	0.10	0.12	0.160±0.029	2±1	8.8±0.9	100.0±0.0
0.88	0.92	0.10	0.12	0.103±0.024	3±2	8.5±1.1	100.0±0.0
0.92	1.00	0.10	0.12	0.030±0.008	13±7	10.4±1.6	100.0±0.0
0.40	0.44	0.12	0.14	1.94±0.17	0±1	4.3±0.3	100.0±0.0
0.44	0.48	0.12	0.14	1.60±0.15	0±1	4.4±0.3	100.0±0.0
0.48	0.52	0.12	0.14	1.33±0.12	0±1	5.4±0.3	100.0±0.0
0.52	0.56	0.12	0.14	0.985±0.100	0±1	5.3±0.3	100.0±0.0
0.56	0.60	0.12	0.14	0.87±0.10	0±1	4.5±0.3	100.0±0.0
0.60	0.64	0.12	0.14	0.83±0.11	0±1	3.9±0.3	100.0±0.0
0.64	0.68	0.12	0.14	0.538±0.078	1±1	4.1±0.3	100.0±0.0
0.68	0.72	0.12	0.14	0.499±0.076	1±1	4.2±0.4	100.0±0.0
0.72	0.76	0.12	0.14	0.276±0.049	1±1	5.0±0.5	100.0±0.0
0.76	0.80	0.12	0.14	0.232±0.051	1±1	3.9±0.4	100.0±0.0
0.80	0.84	0.12	0.14	0.127±0.032	1±1	5.2±0.6	100.0±0.0
0.84	0.88	0.12	0.14	0.133±0.030	2±1	6.6±0.9	100.0±0.0
0.88	0.92	0.12	0.14	0.125±0.038	2±1	5.0±1.0	100.0±0.0
0.92	1.00	0.12	0.14	0.024±0.007	9±6	12.4±2.4	100.0±0.0
0.40	0.44	0.14	0.16	1.22±0.12	0±1	4.5±0.3	100.0±0.0
0.44	0.48	0.14	0.16	1.08±0.12	0±1	4.3±0.3	100.0±0.0

TABLE I. (*Continued*).

x_π		x_N		$d^2\sigma/dx_\pi\,dx_N$	F_{HT}	Acceptance	F_c
Low	High	Low	High	(nb/nucleon)	(%)	(%)	(%)
0.48	0.52	0.14	0.16	0.90±0.11	0±1	3.9±0.3	100.0±0.0
0.52	0.56	0.14	0.16	0.79±0.11	0±1	3.6±0.3	100.0±0.0
0.56	0.60	0.14	0.16	0.617±0.096	0±1	3.3±0.3	100.0±0.0
0.60	0.64	0.14	0.16	0.67±0.11	0±1	2.9±0.3	100.0±0.0
0.64	0.68	0.14	0.16	0.369±0.068	0±1	3.6±0.4	100.0±0.0
0.68	0.72	0.14	0.16	0.309±0.064	1±1	3.3±0.4	100.0±0.0
0.72	0.76	0.14	0.16	0.250±0.055	1±1	3.6±0.4	100.0±0.0
0.76	0.80	0.14	0.16	0.292±0.063	1±1	3.9±0.5	100.0±0.0
0.80	0.84	0.14	0.16	0.147±0.037	1±1	4.9±0.7	100.0±0.0
0.84	0.88	0.14	0.16	0.159±0.041	1±1	5.3±0.9	100.0±0.0
0.88	0.92	0.14	0.16	0.046±0.018	2±1	6.8±1.5	100.0±0.0
0.92	1.00	0.14	0.16	0.014±0.006	7±5	12.0±3.1	100.0±0.0
0.40	0.44	0.16	0.18	1.00±0.12	0±1	3.6±0.3	100.0±0.0
0.44	0.48	0.16	0.18	0.84±0.13	0±1	2.7±0.3	100.0±0.0
0.48	0.52	0.16	0.18	0.74±0.12	0±1	2.6±0.3	100.0±0.0
0.52	0.56	0.16	0.18	0.69±0.11	0±1	2.9±0.3	100.0±0.0
0.56	0.60	0.16	0.18	0.440±0.078	0±1	3.3±0.3	100.0±0.0
0.60	0.64	0.16	0.18	0.341±0.063	0±1	3.9±0.4	100.0±0.0
0.64	0.68	0.16	0.18	0.316±0.058	0±1	4.3±0.4	100.0±0.0
0.68	0.72	0.16	0.18	0.237±0.049	0±1	4.4±0.5	100.0±0.0
0.72	0.76	0.16	0.18	0.182±0.043	0±1	4.5±0.6	100.0±0.0
0.76	0.80	0.16	0.18	0.149±0.039	1±1	4.4±0.7	100.0±0.0
0.80	0.84	0.16	0.18	0.114±0.029	1±1	6.3±0.9	100.0±0.0
0.84	0.88	0.16	0.18	0.071±0.020	1±1	8.8±1.4	100.0±0.0
0.40	0.44	0.18	0.20	0.84±0.14	0±1	2.3±0.2	100.0±0.0
0.44	0.48	0.18	0.20	0.466±0.093	0±1	2.4±0.3	100.0±0.0
0.48	0.52	0.18	0.20	0.466±0.091	0±1	2.6±0.3	100.0±0.0
0.52	0.56	0.18	0.20	0.365±0.069	0±1	3.4±0.3	100.0±0.0
0.56	0.60	0.18	0.20	0.382±0.074	0±1	3.2±0.4	100.0±0.0
0.60	0.64	0.18	0.20	0.306±0.057	0±1	4.3±0.4	100.0±0.0
0.64	0.68	0.18	0.20	0.283±0.055	0±1	4.3±0.5	100.0±0.0
0.68	0.72	0.18	0.20	0.236±0.050	0±1	4.4±0.5	100.0±0.0
0.72	0.76	0.18	0.20	0.110±0.029	0±1	5.1±0.6	100.0±0.0
0.76	0.80	0.18	0.20	0.110±0.031	0±1	5.1±0.7	100.0±0.0
0.80	0.84	0.18	0.20	0.121±0.048	1±1	2.6±0.6	100.0±0.0
0.40	0.44	0.20	0.22	0.63±0.12	0±1	2.1±0.3	100.0±0.0
0.44	0.48	0.20	0.22	0.459±0.087	0±1	2.8±0.3	100.0±0.0
0.48	0.52	0.20	0.22	0.319±0.064	0±1	3.3±0.4	100.0±0.0
0.52	0.56	0.20	0.22	0.299±0.059	0±1	3.8±0.4	100.0±0.0
0.56	0.60	0.20	0.22	0.266±0.056	0±1	3.6±0.4	100.0±0.0
0.60	0.64	0.20	0.22	0.241±0.048	0±1	4.6±0.5	100.0±0.0
0.64	0.68	0.20	0.22	0.192±0.044	0±1	4.2±0.5	100.0±0.0
0.68	0.72	0.20	0.22	0.170±0.038	0±1	5.2±0.6	100.0±0.0
0.72	0.76	0.20	0.22	0.096±0.029	0±1	4.6±0.7	100.0±0.0
0.76	0.80	0.20	0.22	0.081±0.028	0±1	4.3±0.7	100.0±0.0
0.40	0.44	0.22	0.24	0.80±0.16	0±1	1.9±0.3	100.0±0.0
0.44	0.48	0.22	0.24	0.385±0.074	0±1	3.3±0.4	100.0±0.0
0.48	0.52	0.22	0.24	0.399±0.075	0±1	3.4±0.4	100.0±0.0
0.52	0.56	0.22	0.24	0.306±0.066	0±1	3.2±0.4	100.0±0.0
0.56	0.60	0.22	0.24	0.235±0.049	0±1	4.3±0.5	100.0±0.0
0.60	0.64	0.22	0.24	0.203±0.045	0±1	4.3±0.5	100.0±0.0
0.64	0.68	0.22	0.24	0.127±0.031	0±1	5.2±0.6	100.0±0.0
0.68	0.72	0.22	0.24	0.118±0.034	0±1	4.3±0.6	100.0±0.0
0.40	0.44	0.24	0.26	0.445±0.091	0±1	2.7±0.3	100.0±0.0
0.44	0.48	0.24	0.26	0.345±0.070	0±1	3.3±0.4	100.0±0.0
0.48	0.52	0.24	0.26	0.298±0.062	0±1	3.6±0.4	100.0±0.0
0.52	0.56	0.24	0.26	0.188±0.045	0±1	3.8±0.5	100.0±0.0
0.56	0.60	0.24	0.26	0.211±0.049	0±1	3.9±0.5	100.0±0.0

TABLE I. (*Continued*).

x_π		x_N		$d^2\sigma/dx_\pi\, dx_N$	F_{HT}	Acceptance	F_c
Low	High	Low	High	(nb/nucleon)	(%)	(%)	(%)
0.60	0.64	0.24	0.26	0.220±0.053	0±1	3.6±0.5	100.0±0.0
0.64	0.68	0.24	0.26	0.140±0.039	0±1	3.8±0.5	100.0±0.0
0.40	0.44	0.26	0.28	0.331±0.079	0±1	2.5±0.3	100.0±0.0
0.44	0.48	0.26	0.28	0.358±0.073	0±1	3.3±0.4	100.0±0.0
0.48	0.52	0.26	0.28	0.328±0.082	0±1	2.4±0.4	100.0±0.0
0.52	0.56	0.26	0.28	0.284±0.063	0±1	3.4±0.4	100.0±0.0
0.56	0.60	0.26	0.28	0.154±0.041	0±1	3.9±0.5	100.0±0.0
0.60	0.64	0.26	0.28	0.079±0.027	0±1	4.0±0.5	100.0±0.0
0.40	0.44	0.28	0.30	0.287±0.069	0±1	2.8±0.4	100.0±0.0
0.44	0.48	0.28	0.30	0.210±0.055	0±1	3.0±0.4	100.0±0.0
0.48	0.52	0.28	0.30	0.183±0.046	0±1	3.8±0.5	100.0±0.0
0.52	0.56	0.28	0.30	0.124±0.040	0±1	3.0±0.4	100.0±0.0
0.40	0.44	0.30	0.32	0.140±0.050	0±1	2.2±0.4	100.0±0.0
0.44	0.48	0.30	0.32	0.130±0.038	0±1	3.6±0.5	100.0±0.0
0.48	0.52	0.30	0.32	0.130±0.038	0±1	3.6±0.5	100.0±0.0
0.40	0.44	0.32	0.34	0.109±0.035	0±1	3.5±0.5	100.0±0.0
0.44	0.48	0.32	0.34	0.190±0.057	0±1	2.6±0.4	100.0±0.0

V. RESONANCE SUBTRACTION

To investigate the muon-pair continuum below 4.0 GeV/c^2 in mass it was necessary to remove the contribution of the J/ψ and ψ' resonances to the production cross section. This was done by fitting functional forms representing the continuum, J/ψ, and ψ' mass spectra to the raw data. The details of this procedure follow below.

The data were sorted into x_π-x_N bins 0.02 wide in x_π and 0.01 wide in x_N. These bins were further subdivided in x_N to obtain $m_{\mu\mu}^2$ intervals of ~ 0.4 GeV$^2/c^4$ in each x_π interval. For each set of bins in a given x_π interval, a fit was done that matched the raw data to the form

$$C(m_{\mu\mu}) + R(m_{\mu\mu}) + R'(m_{\mu\mu}).$$

The function C was selected empirically to describe the raw data spectrum from the continuum. The J/ψ and ψ' functions R and R' are based on Gaussian forms representing the experimental mass resolution. The form for $R(m_{\mu\mu})$ is empirical, but the need for a complicated form arose because the mass resolution was dependent on the (unknown) location of the production point within the tungsten target, and because of the very large sample of J/ψ events.

The continuum piece $C(m_{\mu\mu})$ is given in terms of three parameters C_1, C_2, and C_3 by

$$C(m_{\mu\mu}) = (m_{\mu\mu} - C_1)^2 \exp[C_2 + C_3 m_{\mu\mu}(1 - 0.0949 m_{\mu\mu}) - 0.158 m_{\mu\mu}^2].$$

The J/ψ component $R(m_{\mu\mu})$ is described by six parameters $R_1, \ldots, R_6$ as

$$R(m_{\mu\mu}) = \begin{cases} A_l \exp(B/R_2^2), & m_{\mu\mu} < 3.0\ \text{GeV}/c^2, \\ A_r[R_5 \exp(B/R_6^2) + \exp(B/0.0289)], & m_{\mu\mu} > 3.15\ \text{GeV}/c^2, \\ R_3 \exp(B/R_4^2), & \text{otherwise}, \end{cases}$$

where $B = -0.5(R_1 - m_{\mu\mu})^2$. The normalization coefficients A_l and A_r follow from the requirement of a smooth match between the three mass regions and are

$$A_l = R_3 \frac{\exp[-0.5(R_1 - 3.0)^2/R_4^2]}{\exp[-0.5(R_1 - 3.0)^2/R_2^2]},$$

and

$$A_r = \frac{R_3 \exp[-0.5(R_1 - 3.15)^2/R_4^2]}{R_5 \exp[-0.5(R_1 - 3.15)^2/R_6^2] + \exp[-0.5(R_1 - 3.15)^2/0.0289]}.$$

The ψ' piece $R'(m_{\mu\mu})$ is given by

$$R'(m_{\mu\mu}) = R_1' \exp[-0.5(3.69 - m_{\mu\mu})^2/(0.163)^2],$$

where R_1' is allowed to vary. In each case $m_{\mu\mu}$ is in GeV/c^2.

The fit to the resonance and continuum forms was performed over the range 2.0 GeV/c^2 < $m_{\mu\mu}$ < 6.0 GeV/c^2 for each 0.02-wide strip in x_π. Once the 10 variable parameters describing the mass spectrum for a particular strip were determined, the fraction F_c of data at a given

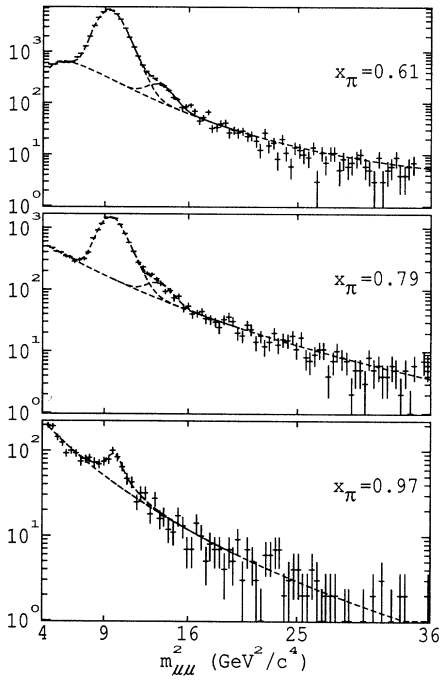

FIG. 1. Raw mass spectra at three values of x_π. The dashed curves show the fits to the J/ψ, ψ', and continuum components.

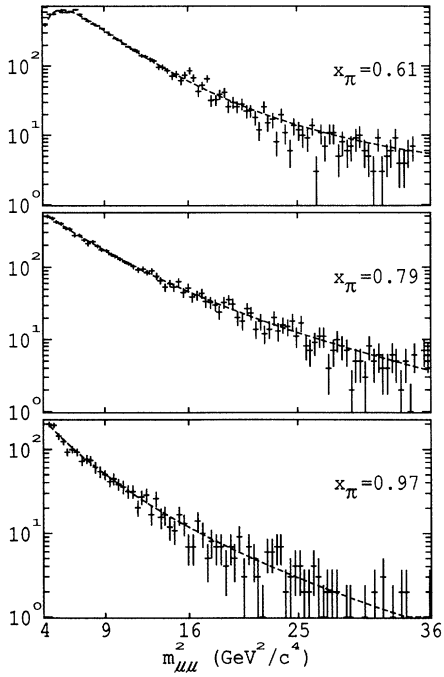

FIG. 2. Raw mass spectra after resonance subtraction. The curves are the continuum component.

mass that was due to the continuum was taken to be

$$F_c = \frac{C(m_{\mu\mu})}{C(m_{\mu\mu}) + R(m_{\mu\mu}) + R'(m_{\mu\mu})}.$$

Raw mass spectra with J/ψ, ψ', and continuum pieces shown separately are presented in Fig. 1 for three representative values of x_π. Figure 2 shows the result of the resonance subtraction for three values of x_π; each point on the plot is the product of the raw data and the value of F_c corresponding to that particular bin. As x_π increases, the fraction of the raw data attributed to the continuum at the J/ψ peak increases from $\sim$ 5% at $x_\pi = 0.6$ to $\sim$ 70% at $x_\pi = 0.99$. Thus an error in the subtraction procedure would be more likely to affect the continuum signal at moderate than at large x_π.

Because of the large amount of J/ψ present at low x_π and the low experimental acceptance in the low-mass low-x_π region, the use of the resonance subtraction was confined to x_π greater than $\sim$ 0.6. For the latter case a clear continuum signal is evident for masses below 2.5 GeV/c^2, so that the fit to the continuum function C is well determined throughout the resonance region. Data with $0.4 < x_\pi < 0.6$ were included in the analysis only if $m_{\mu\mu} > 4$ GeV/c^2, and no resonance subtraction was attempted in this case.

The statistical uncertainty of the continuum function F_c was computed using a Monte Carlo method: First, 100 simulated raw mass spectra were produced for each strip in x_π based on Poisson deviates about the fit to the observed mass spectra. Then, we assigned statistical errors to F_c in each strip equal to the standard deviation of the 100 simulated F_c. The continuum fractions and associated uncertainties are reported for bins of x_π-x_N in the last column of Table I. In many cases the error on the measured cross section is dominated by the uncertainty in the continuum fraction.

The uncertainty in the subtraction procedure is primarily due to uncertainty in the form of the continuum function F_c. The "statistical" uncertainty just discussed automatically includes an estimate of uncertainty in the form of F_c within the range of parameters allowed by our algorithm. Because of the generality of the form of F_c, this error estimate should include the majority of any systematic effects. A sense of remaining systematic effects can be had from a comparison with the next-to-last version of the procedure. In that, a discernible excess of resonance events remained in the mass region 3.4–3.5 GeV/c^2, amounting to about 10% of the continuum there. When the cross-section analysis described in Sec. VI was performed using the contaminated continuum, the χ^2 of fit 21 of Table II was 251 rather than 248 as in the final analysis, and parameter β was fit as 3.9 ± 0.5 rather than 4.4 ± 0.6. We believe that any remaining systematic effects in the final subtraction procedure are smaller than the difference between this and the next-to-last version.

Various cross sections are presented in Appendix F for the J/ψ and ψ' resonances that have been isolated by the above procedure.

TABLE II. Fits to the measured cross section $d^2\sigma/dx_\pi\, dx_N$. Fit order includes naive, leading log (LLOG), and next-to-leading log (NLL). Fit regions are shown in Fig. 3.

Fit no.	Region	Order	Higher twist	χ^2	N_{DF}	Probability	α	β
1	A	Naive	none	166	170	0.57		
2	A	LLOG	none	168	170	0.53		
3	A	NLL	none	168	170	0.53		
4	B	Naive	none	296	193	3×10^{-6}		
5	B	LLOG	none	259	193	0.001		
6	B	NLL	none	266	193	4×10^{-4}		
7	C	Naive	none	623	214	1×10^{-41}		
8	C	LLOG	none	463	214	2×10^{-20}		
9	C	NLL	none	464	214	2×10^{-20}		
10	B	Naive	$x_\pi^2/m_{\mu\mu}^2$	222	192	0.07		
11	B	LLOG	$x_\pi^2/m_{\mu\mu}^2$	217	192	0.10		
12	B	NLL	$x_\pi^2/m_{\mu\mu}^2$	219	192	0.09		
13	C	Naive	$x_\pi^2/m_{\mu\mu}^2$	344	213	3×10^{-8}		
14	C	LLOG	$x_\pi^2/m_{\mu\mu}^2$	292	213	3×10^{-4}		
15	C	NLL	$x_\pi^2/m_{\mu\mu}^2$	292	213	3×10^{-4}		
16	B	Naive	$x_\pi^\alpha/m_{\mu\mu}^\beta$	211	190	0.14	3.0 ± 1.5	4.4 ± 1.2
17	B	LLOG	$x_\pi^\alpha/m_{\mu\mu}^\beta$	205	190	0.22	5.6 ± 2.1	4.8 ± 1.4
18	B	NLL	$x_\pi^\alpha/m_{\mu\mu}^\beta$	206	190	0.20	5.6 ± 2.0	4.7 ± 1.3
19	C	Naive	$x_\pi^\alpha/m_{\mu\mu}^\beta$	266	211	0.006	2.0 ± 0.4	4.4 ± 0.6
20	C	LLOG	$x_\pi^\alpha/m_{\mu\mu}^\beta$	247	211	0.05	2.4 ± 0.6	4.5 ± 0.7
21	C	NLL	$x_\pi^\alpha/m_{\mu\mu}^\beta$	248	211	0.04	2.8 ± 0.6	4.4 ± 0.6

VI. DISTRIBUTIONS IN x_π AND x_N

Table I contains our measured cross sections $d^2\sigma/dx_\pi\, dx_N$ in each x_π-x_N bin used in the analyses below. The fraction of the cross section that we attribute to higher-twist effects (see Sec. VI C below) is also given for each bin. The errors shown in this table are statistical only; there is an overall normalization uncertainty of 15% in the absolute cross section that has no effect on the shape of the measured distributions.

Figure 3 illustrates the region of the x_π-x_N plane covered by these measurements. Our measurements in region A prove to be consistent with QCD analyses at lowest twist, while the data in regions B and C appear to indicate the presence of higher-twist effects that become prominent at large x_π and low mass. There are 4.3×10^4, 5.0×10^4, and 8.9×10^4 events in regions A, B, and C, respectively, after removal of the resonances.

A. Naive analysis

The Drell-Yan cross section in lowest order for $\pi^- N \to \mu^+\mu^- X$, with the neglect of the pion sea, is given by

$$\frac{d^2\sigma}{dx_\pi\, dx_N} = \frac{4\pi\alpha^2}{9s} \frac{F(x_\pi)G(x_N)}{(x_\pi x_N)^2}.$$

The pion structure function $F(x_\pi)$ is just x_π times the valence-quark distribution of the pion (the valence-quark and valence-antiquark distributions are assumed to be equal in the pion, due to G-parity invariance). The measurement of the pion sea- and valence-quark distributions by Badier *et al.* [13] showed that the pion sea was $\sim 1.5\%$ of the pion valence at $x_\pi = 0.4$; this sea-valence ratio decreased rapidly with increasing x_π. We have required $x_\pi > 0.4$ in this analysis. Since the effect of the pion sea on the cross section in this region is small compared to experimental errors, we have neglected the effect of the pion sea in all analysis presented here.

The nucleon structure function $G(x_N)$ is the sum of sea and valence parts:

$$G(x_N) = \frac{x_N}{9}\,[4(0.5+\epsilon)u(x_N) + 4(0.5-\epsilon)d(x_N) + 5S(x_N)]\,,$$

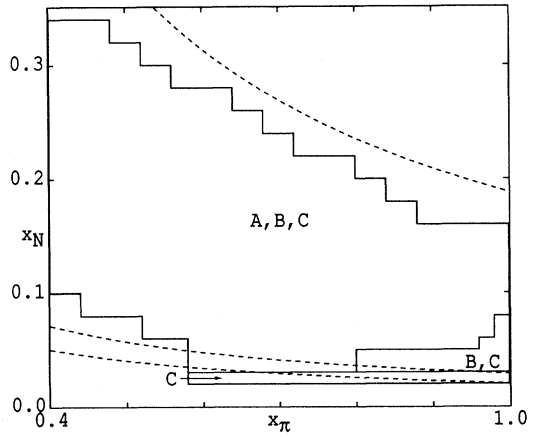

FIG. 3. The three regions A, B, and C in x_π-x_N space used in fitting the data. Also shown are curves corresponding to (from top to bottom) the Υ, ψ', and J/ψ resonances. Region A is a subset of region B, which is a subset of region C. There are 4.3×10^4, 5.0×10^4, and 8.9×10^4 events in regions A, B, and C, respectively, after removal of the resonances.

where u and d correspond to the proton u-valence- and d-valence-quark distributions, respectively, and

$$S = (0.5 + 0.6\epsilon)\bar{u} + (0.5 - 0.6\epsilon)\bar{d}$$

is the average nucleon sea. Here $\epsilon = Z/A - \frac{1}{2}$ is the deviation of the target from isoscalar; $\epsilon = -0.095$ for the tungsten target used in this experiment. In the case of the nucleon it is assumed that the u- and d-quark distributions in the proton are the same as the d- and u-quark distributions in the neutron. No heavy-quark contribution appears because the pion contains no heavy valence quarks.

The exact forms that we used for the nucleon quark distributions and corresponding sum rules are given in Appendix A. All nucleon parton distributions are based on a parametrization of $u(x_N)$, the proton u-valence-quark distribution, via various constraints derived from experiment. The form used for the pion valence-quark distribution is given in Appendix B. Because our data are limited to $x_\pi > 0.4$, the usual sum rules cannot be usefully applied to the pion valence distribution. The sum rules for the nucleon quark distributions are enforced, however, as extra constraints on the nucleon sea and valence distributions.

The forms used for $u(x_N)$ and $F(x_\pi)$ were general enough to represent any smooth function consistent with the applied constraints (no power-law behavior was assumed to hold). This represents a departure from our procedure in Ref. [10] where $x^\alpha(1-x)^\beta$ forms were used for both $u(x_N)$ and $F(x_\pi)$. In all fits presented here, a normalization factor was included as a free parameter since the pion sum rules were not enforced; if the pion sum rules could be used to give the normalization of $F(x_\pi)$, the normalization factor would become the K factor (the ratio of experimentally measured to theoretically predicted cross sections). Our previous paper [10] reported a K factor based on $x_\pi > 0.2$, $m_{\mu\mu} > 4.05$ GeV/c^2; since the resonance subtraction is used here only for $x_\pi > 0.6$, no improvement on the previously reported K factor was possible in this analysis.

First, a fit was performed that optimized the pion and nucleon quark distributions to reproduce the measured cross section, the relation between the quark distributions and cross section being the lowest-order (naive) expression given above. To obtain a reasonable χ^2 per degree of freedom for this fit, it was necessary to remove data bins at low mass and high x_π; there was a larger cross section in this region than was consistent with the naive model. Figure 4 shows the fit residuals for all bins in region C (refer to Fig. 3), but only the bins in region A, enclosed in solid lines, were used in the fit. For the fit over region A, the χ^2 was 166 for 170 degrees of freedom, corresponding to a probability of 57%. A summary of the qualities of this and subsequent fits is given in Table II, where this fit is called fit 1.

When all bins in region C were included in the fit (fit 7 of Table II), the χ^2 increased to 623 for 214 degrees of freedom. The necessity of excluding a region at low mass and high x_π was described by us in Ref. [10] as a "low-mass anomaly." It was the existence of that "anomaly" that prompted this study.

Because the naive model is clearly inadequate to describe the data over all of region C, we defer discussion of the interpretation of the fits until various corrections have been considered.

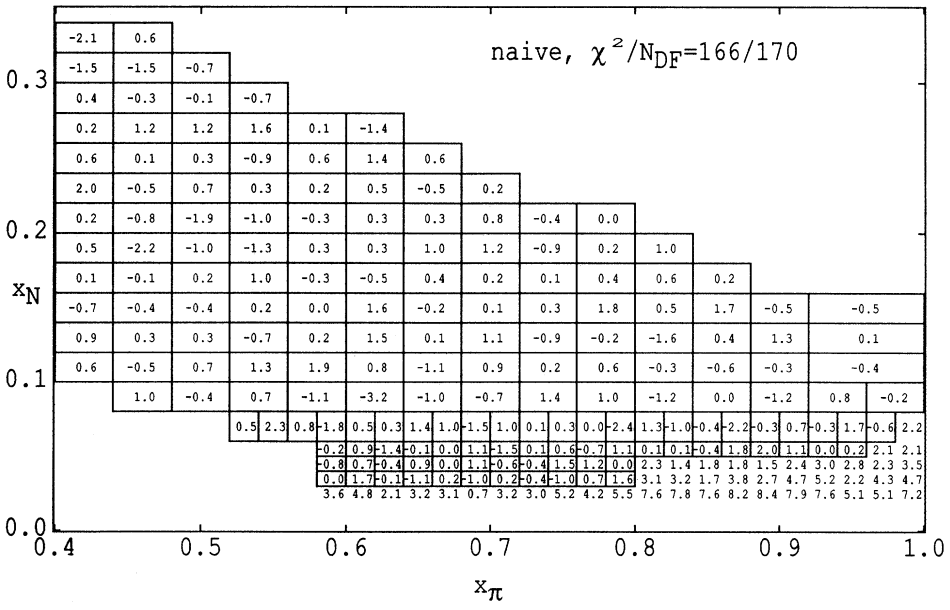

FIG. 4. Residuals of fit 1 of Table II to data in region A using the naive form of the cross section. Also shown are residuals outside region A that are not included in the fit and do not contribute to χ^2. No higher-twist term is included in this fit.

B. Higher-order QCD corrections

We next performed fits to the cross-section data at leading-log and next-to-leading-log order in the Drell-Yan model. The procedures used to calculate the (lowest-twist) QCD corrections to the cross section are described in Appendixes C and D. The quality of the resulting fits is essentially unchanged from the naive case. On fitting over region A, the χ^2 was 168 for 170 degrees of freedom (probability 53%) in both the leading-log (fit 2) and next-to-leading-log (fit 3) cases.

Although the addition of QCD corrections improves the fit quality in region A only slightly, the resultant nucleon structure function $G(x_N)$ changes significantly. Figure 5 shows the $G(x_N)$ produced by the fit to the data using the naive Drell-Yan model (fit 1). Figure 5 also shows $G(x_N)$, evaluated at a mass of 5.16 GeV/c^2, resulting from fit 3 which includes corrections up to next-to-leading-log order. The $G(x_N)$ associated with the leading-log fit (fit 2) was nearly identical to the next-to-leading-log fit, and is not shown.

To assess the statistical significance of our measurements of $G(x_N)$ [and also $F(x_\pi)$] we studied the variations of these in analyses of several sets of simulated data. In each bin in the x_π-x_N plane, the number of simulated events was selected randomly from a Poisson distribution based on the observed number of events (more precisely, on the number of events corresponding to the best-fitted cross section for each bin). Values of the structure functions were obtained from fits to 100 such sets of simulated data. Then the variance of the structure functions were calculated at each x_N or x_π, which we take as a good representation of the accuracy of the fit.

Figure 5 shows the $\pm 1\sigma$ confidence bands surrounding the results for $G(x_N)$ from fits 1 and 3. The nucleon structure function from fit 1 is significantly steeper than the QCD-corrected fit 3 for $x_N < 0.1$. This affects the size of the structure function at larger x_N via the sum rules that the parton distributions satisfy.

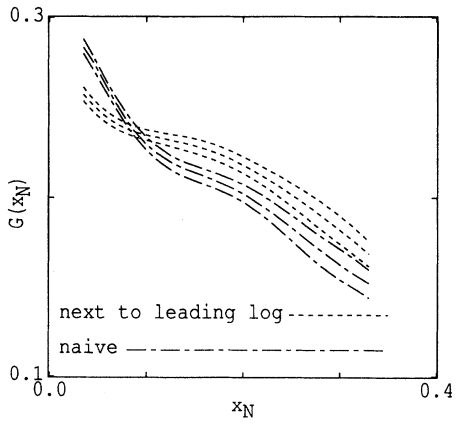

FIG. 5. Nucleon structure function $G(x_N)$ resulting from the naive fit 1 to the cross section over region A (dash-dot curve), and that from fit 3 at next-to-leading-log order (dashed curve) over the same region. Also shown are $\pm 1\sigma$ statistical-error bands.

These results were obtained from analyses of region A only. When all bins in region C are included the χ^2's of the fits change to 463 for 214 degrees of freedom at leading-log order (fit 8) and 464 for 214 degrees of freedom at next-to-leading-log order (fit 9). Thus, the excess cross section observed in the low-mass high-x_π region is not consistent with the Drell-Yan model even with QCD corrections at next-to-leading-log order.

C. Higher-twist effects

To obtain good fit quality over regions B and C we next considered higher-twist effects that are predicted to be prominent at low mass and large x_π.

To add higher twist to the model of the cross section we first used the prediction of Brodsky, Berger, and Lepage [15]: a term proportional to $x_\pi^2/m_{\mu\mu}^2$ was added to the pion structure function. This is straightforward in the naive case (see Appendix B). In the leading-log and next-to-leading-log cases we did not allow the higher-twist piece (or its generalization below) to evolve according to the Altarelli-Parisi equations. Thus our higher-twist term is not subject to leading-log QCD corrections.

As an example of the resulting fit quality, consider the next-to-leading-log fit over region B with a higher-twist term proportional to $x_\pi^2/m_{\mu\mu}^2$. The addition of the higher-twist term improves the fit in the low-mass high-x_π region, but there is still a residual excess of measured cross section (especially if one extends the fit to region C). The χ^2 for such fits over region B are 222, 217, and 219 for 192 degrees of freedom for the naive, leading-log, and next-to-leading-log fits, respectively (see fits 10, 11, and 12 of Table II). The nucleon structure functions $G(x_N)$ from these fits did not change significantly from those shown in Fig. 5. When all bins in region C were included, the χ^2 became 344, 292, and 292 for 213 degrees of freedom for fits 13, 14, and 15, respectively.

Because the data suggest that the form $x_\pi^2/m_{\mu\mu}^2$ for higher twist does not fit the measured cross section at the lowest value of mass considered, fits were performed using the form $x_\pi^\alpha/m_{\mu\mu}^\beta$ where α and β were allowed to vary. We refer to this form as a generalized higher-twist correction. This form is only loosely modeled after the general form of higher-twist effects [6], which suggests that β should be an even integer. Fits 16–21 of Table II illustrate the progression of fit quality from the naive model to the inclusion of the next-to-leading-log corrections, all with generalized higher-twist terms as well.

The optimum values of α and β resulting from fit 21 at next-to-leading-log order over region C are $\alpha = 2.8 \pm 0.6$ and $\beta = 4.4 \pm 0.6$. The fit region, χ^2, and residuals are shown in Fig. 6. While the χ^2 probability of fit 21 is only 4%, Fig. 6 shows that if there is any concentration of high residuals it is for low x_N and moderate x_π, where the J/ψ signal is much larger than that for the continuum and the resonance subtraction is difficult. As another illustration of the quality of this fit, Fig. 7 shows measured cross sections from Table I and curves derived from the fit. The dashed curve includes the generalized higher-twist term while the dotted curve does not. For low x_N the

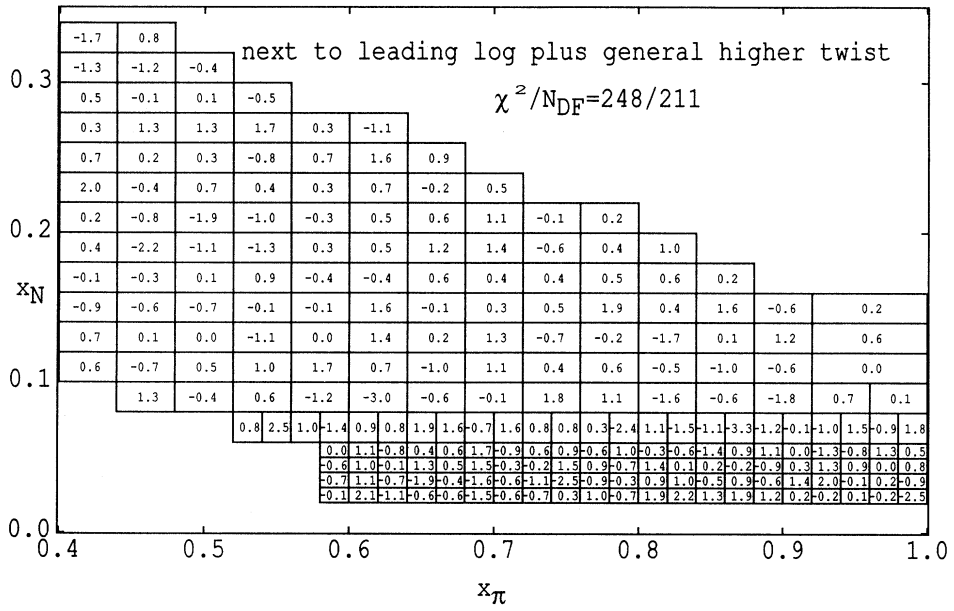

FIG. 6. Residuals of fit 21 to data in region C using the next-to-leading-log form of the cross section ($x_\pi^\alpha/m_{\mu\mu}^\beta$ higher-twist term).

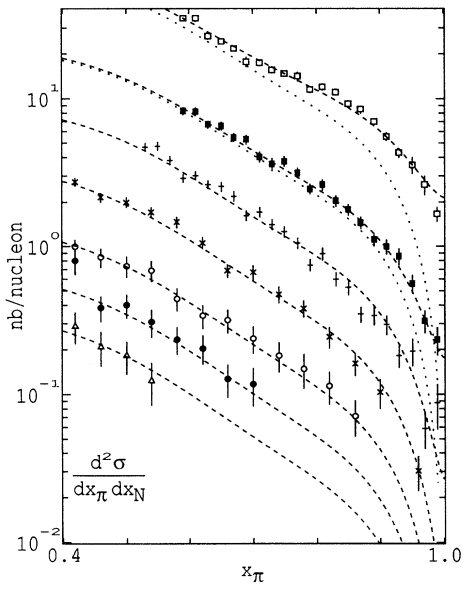

FIG. 7. Cross sections $d^2\sigma/dx_\pi\, dx_N$ in nb/nucleon from Table I. From top to bottom the bands are $x_N = 0.025$, $x_N = 0.045$, $x_N = 0.07$, $x_N = 0.11$, $x_N = 0.17$, $x_N = 0.23$, and $x_N = 0.29$. For clarity a few x_N bins from the table are omitted. Also shown are dashed curves resulting from fit 21 to the cross sections using the next-to-leading-log form with generalized higher twist. The dotted curves show the contribution from the Drell-Yan cross section plus QCD corrections at lowest twist only, in regions where the higher-twist component is significant.

higher-twist contribution is prominent over a wide range of x_π.

The nucleon structure function $G(x_N)$ from fit 21 is shown in Fig. 8 (curve with long and short dashes), along with an estimate of $G(x_N)$ (dashed curve) from recent fits to parton distributions from analysis of deeply inelastic scattering experiments at next-to-leading-log order [16]. The error bands on our measurement of $G(x_N)$ were estimated with the procedure described in the previous subsection. Also shown are the separate contributions to $G(x_N)$ from sea and valence quarks. The difference between our measurement and the extrapolation from deeply inelastic scattering appears to be due to our larger results for the sea-quark distribution at low x_N.

We also wish to illustrate the detailed character of the pion structure function extracted from these fits. For the case of the naive model we simply report in Table V of Appendix B the numerical values for the parameters of fit 16 which includes the generalized higher-twist effect over region B. Figure 9 shows the corresponding pion structure function at a mass of 5.16 GeV/c^2, without indication of the errors.

Figure 10 illustrates $\pm 1\sigma$ intervals about the pion structure function from fit 20 over region C including both leading-log corrections and a generalized higher-twist term. It is shown for three values of $m_{\mu\mu}$ to indicate the mass dependence due to the QCD corrections; the nonscaling nature of $F(x_\pi)$ is very significant at high x_π and is largely due to the higher-twist effect rather than the QCD evolution of the parton distributions.

Figure 9 also shows the non-higher-twist part of the pion structure functions from fit 21 over region C including both next-to-leading-log corrections and a gener-

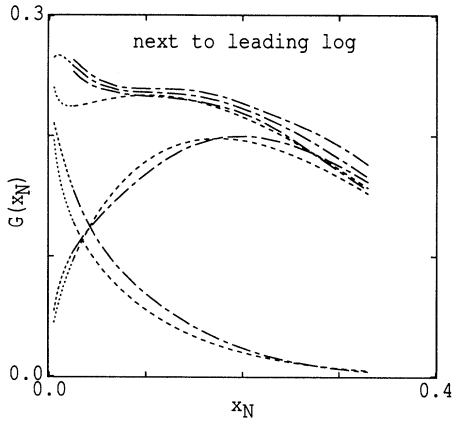

FIG. 8. The nucleon structure function $G(x_N)$ from fit 21 (dashed-dot curve) over region C at next-to-leading-log order plus generalized higher twist. The $\pm 1\sigma$ statistical-error bands are also shown over the interval $0.025 < x_N < 0.33$ for which there are data. The extrapolation of the structure function to lower values of x_N is indicated, according to the parametrization of Appendix E. The separate components of the structure function from sea and valence quarks are shown on the lower part of the figure. For comparison the structure functions calculated from set SN-DIS of a recent comprehensive analysis at next-to-leading-log order by Morfin and Tung [16] are shown as the dashed curves.

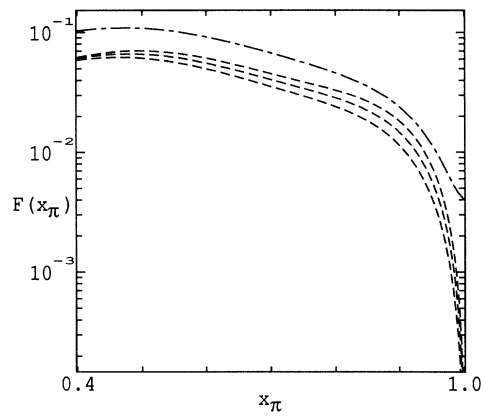

FIG. 9. The uppermost (dash-dot) curve is the pion structure function from fit 16 over region B using the naive model plus generalized higher twist. The higher-twist term was evaluated at a mass of 5.16 GeV/c^2. The lower three (dashed) curves are from fit 21 over region C at next-to-leading-log order plus generalized higher twist; however, the contribution from the higher-twist term is not shown. The dashed curves are for $m_{\mu\mu} = 3.5$, 5.16, and 8.5 GeV/c^2 from top to bottom. The normalization of the naive pion structure function is larger than that of the next-to-leading-log structure functions because in our naive analysis the K factor is absorbed into the pion structure function.

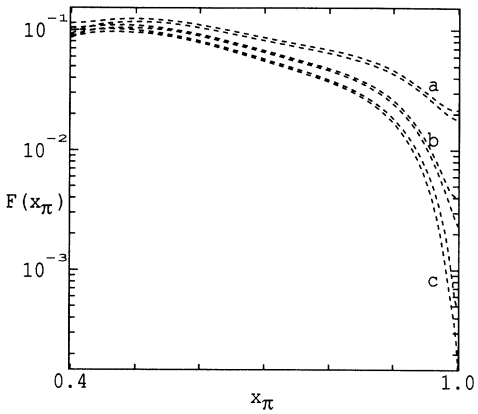

FIG. 10. Pion structure functions from fit 20 over region C at leading-log order, including the generalized higher-twist term $x_\pi^\alpha / m_{\mu\mu}^\beta$. Bands a, b, and c correspond to $m_{\mu\mu} = 3.5$, 5.16, and 8.5 GeV/c^2, respectively. The band structures represent $\pm 1\sigma$ confidence intervals about the best fit, as described in the text.

alized higher-twist term, again for three values of $m_{\mu\mu}$. Here the mass dependence is only due to the QCD evolution of the parton distributions. The normalization of the naive pion structure function shown in Fig. 9 is larger than that of the next-to-leading-log structure functions because in our naive analysis the K factor is absorbed into the pion structure function.

In comparing the 21 fits summarized in Table II, several conclusions may be drawn. The data in region A (see Fig. 3) are adequately described by the naive, leading-log, and next-to-leading-log models (fits 1–3) without any higher-twist corrections; the same cannot be said of regions B or C. Adding a higher-twist term proportional to $x_\pi^2 / m_{\mu\mu}^2$ in the pion structure function (fits 10–12) reduced the χ^2 for the fit to region B by ~ 50 (compared to fits 4–6); this corresponds to a statistical significance of about 7 standard deviations for this higher-twist term in region B.

The $x_\pi^2 / m_{\mu\mu}^2$ term clearly is not adequate to describe region C; a significant improvement in the fit to the data over this region was obtained by using the more general form $x_\pi^\alpha / m_{\mu\mu}^\beta$, where α and β were allowed to vary. The fit quality over region B was also improved by using the more general form for higher twist. The χ^2 for region C improved by ~ 200, comparing fits 7–9 with no higher twist and fits 19–21 with generalized higher twist, indicating a statistical significance of about 14 standard deviations for the higher-twist effects. Even comparing fits 19–21 over region C with generalized higher twist vs fits 13–15 with the basic higher-twist term $\sim x_\pi^2 / m_{\mu\mu}^2$, the χ^2 improved by ~ 40, indicating a statistical significance of about 6 standard deviations for the generalized higher-twist effect over the basic effect. Fits 16–21 over regions B and C are consistent with a $x_\pi^\alpha / m_{\mu\mu}^4$ mass dependence for the higher-twist term in the cross section; however, α is more strongly dependent on both the fit region and the order of QCD corrections. There is a positive correlation between the α and β parameters; in each fit, when β is

TABLE III. Fits to the measured cross section $d^2\sigma/dx_\pi\,dx_N$ over region C at next-to-leading-log order including the modified higher-twist term $x_\pi^2(A_1/\tau + A_2/\tau^2 + A_3/\tau^3)$, where $\tau = m_{\mu\mu}^2/s$.

Fit no.	χ^2	N_{DF}	Probability	A_1	A_2	A_3
22	250.4	213	0.04	0 (fixed)	$(5.43 \pm 0.41) \times 10^{-5}$	0 (fixed)
23	250.3	212	0.04	$(-1.0 \pm 4.0) \times 10^{-4}$	$(5.63 \pm 0.90) \times 10^{-5}$	0 (fixed)
24	248.7	211	0.04	$(-7.9 \pm 6.7) \times 10^{-4}$	$(9.4 \pm 3.1) \times 10^{-5}$	$(-5.3 \pm 4.1) \times 10^{-7}$

fixed at 4.0, α decreases by ~ 0.5.

We attempted to improve the fit quality further by using the form

$$x_\pi^2(A_1/\tau + A_2/\tau^2 + A_3/\tau^3),$$

where $\tau = m_{\mu\mu}^2/s$, for the higher-twist term in the pion structure function. This form is better motivated by theories of higher twist [6], in which a series of power-law corrections in τ^{-n} is expected. With this form we fit only over region C at next-to-leading-log order to find the results summarized in Table III. Fits 21 and 22 provide similar evidence for a higher-twist term proportional to $1/m_{\mu\mu}^4$. Fits 23 and 24 give no strong evidence of any higher-twist terms proportional to $1/m_{\mu\mu}^2$ or $1/m_{\mu\mu}^6$ in addition to the observed $1/m_{\mu\mu}^4$ dependence. However, these additional terms may be present in the cross section at levels below the sensitivity of our measurement.

Figure 11, as well as Table I, shows the fraction F_{HT} in percent of the muon-pair-production cross section due to higher-twist effects, as a function of x_π and x_N. This fraction is based on fit 21 to the data using next-to-leading-log order over region C, with $x_\pi^\alpha/m_{\mu\mu}^\beta$ for the higher-twist term. The fraction F_{HT} is given by $F_{HT} = \sigma_{HT}/(\sigma_{DY} + \sigma_{HT})$, where σ_{DY} and σ_{HT} are the lowest-twist and higher-twist components of the cross section, respectively. The higher-twist contribution to the cross section, negligible at high mass and low x_π, increases to $\sim 95\%$ at the low mass and high x_π.

Appendix E gives a parametrization of the pion and nucleon distributions and K function from fit 21. This provides a parametrization of $d^2\sigma/dx_\pi\,dx_N$ and the size of the higher-twist contribution in that region.

A broad result of the above analyses should not be lost sight of. The present work is the first study of the muon-pair continuum in the 3–4-GeV/c^2 mass range. The cross section over most of this region is well fit by the Drell-Yan model (with next-to-leading-log corrections), and the observed deviations from this are consistent with higher-twist effects.

D. Higher-twist effects at 80 GeV/c

As described in Ref. [14], this experiment has also taken data using an 80-GeV/c π^- beam; our analysis of these data was published in Ref. [9]. That analysis treated $\mu^+\mu^-$ pairs with $m_{\mu\mu} > 4.0$ GeV/c^2 and $x_F > 0.2$; higher-twist effects in the $d\sigma/d\cos\theta$ distribution were significant for $x_\pi > 0.9$ in that data set. In

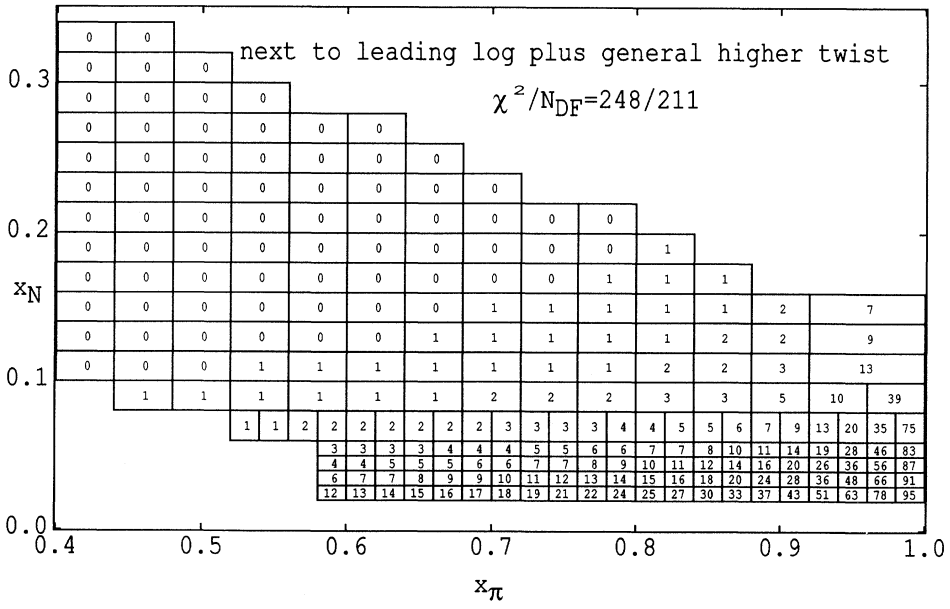

FIG. 11. The fraction F_{HT} (in percent) of the cross section $d^2\sigma/dx_\pi\,dx_N$ due to higher-twist effects, based on fit 21.

view of the minimum muon-pair mass of 4 GeV/c^2 no subtraction of the J/ψ and ψ' resonances was needed or made. The form used then for the pion structure function was

$$F(x_\pi) = x_\pi^a[(1-x_\pi)^b + c],$$

where a, b, and c were parameters determined by fitting to the data. Those fits used naive forms for both the pion and nucleon structure functions, and the term associated with the higher-twist effects (cx_π^a) also had no mass dependence.

At that time it was observed that the nucleon structure function determined by those fits was steeper than that found by deeply inelastic lepton scattering experiments. In view of the $1/m_{\mu\mu}^4$ dependence of the higher-twist effects observed in our 253-GeV/c data, we have refit the 80-GeV/c data using an $x_\pi^\alpha/m_{\mu\mu}^\beta$ form for the higher-twist piece as above. As we have only 4000 muon pairs with $m_{\mu\mu} > 4.0$ GeV/c^2 in our 80-GeV/c data sample we did not fit for both the pion and nucleon structure functions. Rather, we have used the Duke-Owens [17] leading-log parametrizations (set 1) for the nucleon structure function, and fit only for the pion structure function.

The fits were done using the leading-log form of the cross section; the pion structure function was handled exactly as in the 253-GeV/c leading-log fits. When the higher-twist term $x_\pi^\alpha/m_{\mu\mu}^\beta$ was included in the pion structure function, the result of the fit was $\alpha = -2.2 \pm 0.8$, $\beta = 5.3 \pm 1.9$ with $\chi^2 = 107$ for 80 degrees of freedom. This is consistent with the $1/m_{\mu\mu}^4$ dependence seen in the 253-GeV/c data; however, the statistical power at 80 GeV/c is much less because of the smaller data sample.

When the higher-twist term was eliminated, or even when it was taken to be $\propto x_\pi^{0.4}/m_{\mu\mu}^0$ as in Ref. [9], the fit gave $\chi^2 = 145$ for 83 degrees of freedom. This reflects the incompatibility of the 80-GeV/c data with a cross-section model based on nucleon structure functions from deeply inelastic lepton scattering combined with a pion structure function with only the $x_\pi^{0.4}/m_{\mu\mu}^0$ higher-twist term. It also indicates a statistical significance of ~ 6 standard deviations for the existence of generalized higher-twist effects in the 80-GeV/c data, compared to the simplified hypothesis of Ref. [9]. Thus the use of the generalized higher-twist term restores reasonable compatibility (χ^2 probability of 2.4%) of the data with nucleon structure functions from deeply inelastic scattering experiments.

VII. DISTRIBUTION IN $\cos\theta$

At lowest order in the Drell-Yan model [2], annihilation of spin-$\frac{1}{2}$ partons results in

$$\frac{d\sigma}{d\cos\theta} \propto 1 + \cos^2\theta.$$

This is largely unchanged by the addition of QCD corrections at lowest twist [18]. When higher-twist corrections are considered, Berger and Brodsky have shown [5] that

$$\frac{d\sigma}{d\cos\theta} \propto 1 - \cos^2\theta$$

is expected for low mass as $x_\pi \to 1$. This suggests that the angular distribution be parametrized as

$$\frac{d^3\sigma}{dx_\pi\, dx_N\, d\cos\theta} = \frac{d^2\sigma}{dx_\pi\, dx_N}\frac{1+\lambda\cos^2\theta}{2+2\lambda/3},$$

where the parameter λ is a function of x_π and x_N.

The data were divided into 6 bins in $\cos\theta$ covering the range $-0.75 < \cos\theta < 0.85$. To investigate the $\cos\theta$ distribution below 4.0 GeV/c^2 in muon-pair mass, the resonance subtraction described above was performed separately in each of the $\cos\theta$ bins. Figure 12 shows the acceptance-corrected $\cos\theta$ spectra for representative ranges in x_π and x_N. The requirement that $\cos\theta > -0.75$ does not completely eliminate the background from beam-associated negative muons, but the results are not significantly altered by the residual background. For each range in x_π and x_N, a value for λ was determined that best represented the data. All the values thus determined are displayed on an x_π-x_N grid in Fig. 13.

At high mass and low x_π the data are consistent with $\lambda = 1$, but in the low-mass, high-x_π region the data strongly support the $\lambda \to -1$ prediction of the higher-twist model. This measurement is consistent with our previous work [8–10], and with the measurements of $d\sigma/d\cos\theta$ by Badier *et al.* [19] (NA3 experiment) and Guanziroli *et al.* [20] (NA10 experiment) in the region of x_π-x_N space covered by those experiments. However, neither NA3 nor NA10 had sufficient acceptance in the

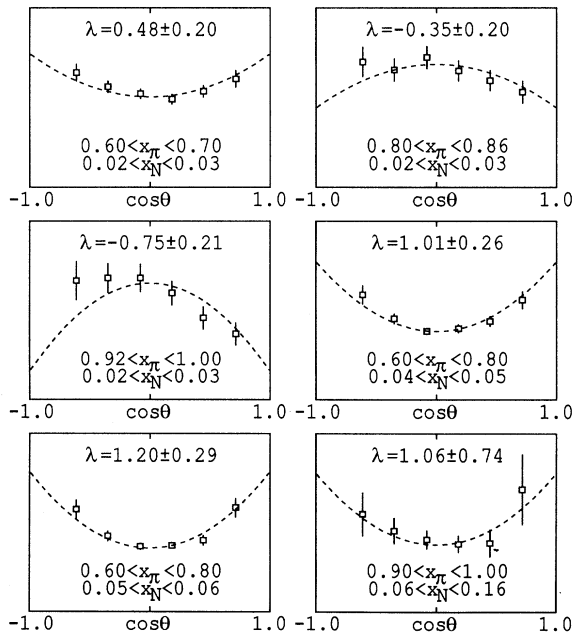

FIG. 12. The measured cross section $d\sigma/d\cos\theta$ at selected values of x_π and x_N. The curves are fits of the form $d\sigma/d\cos\theta \propto 1 + \lambda\cos^2\theta$, yielding the values of λ as shown.

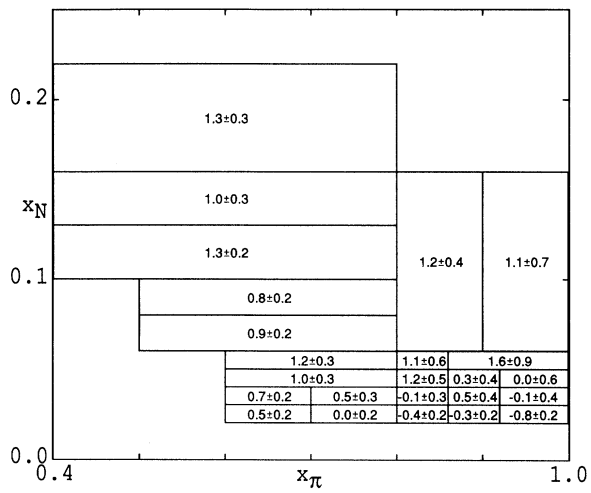

FIG. 13. The measured value of λ from fits of the form $d\sigma/d\cos\theta \propto 1 + \lambda\cos^2\theta$ for each x_π-x_N bin.

low-mass, high-x_π region to test the higher-twist prediction concerning λ. It should also be noted that the NA3 angular distributions were confined to the region above 4.5 GeV/c^2 in mass; in our own data the variations in λ are barely discernible in this mass region.

If higher twist is responsible for $\lambda \to -1$ and also responsible for a mass-dependent term in the pion structure function, the measured λ will be related to the higher-twist fraction of Table I. We write

$$\frac{1}{\sigma}\frac{d\sigma}{d\cos\theta} = (1 - F_{\rm HT})\frac{1 + \lambda_{\rm DY}\cos^2\theta}{2 + 2\lambda_{\rm DY}/3} + F_{\rm HT}\frac{1 + \lambda_{\rm HT}\cos^2\theta}{2 + 2\lambda_{\rm HT}/3},$$

where $\lambda_{\rm DY}$ and $\lambda_{\rm HT}$ are constants. Then

$$\lambda = \frac{\lambda_{\rm HT}\lambda_{\rm DY} + 3F_{\rm HT}\lambda_{\rm HT} + 3(1 - F_{\rm HT})\lambda_{\rm DY}}{3 + F_{\rm HT}\lambda_{\rm DY} + (1 - F_{\rm HT})\lambda_{\rm HT}},$$

where $F_{\rm HT}$ is the higher-twist fraction ($F_{\rm HT}$ and λ are functions of x_π and x_N).

A fit of the measured λ of Fig. 13 to the above form (using $F_{\rm HT}$ of Table I) yields $\lambda_{\rm DY} = 1.20 \pm 0.10$ and $\lambda_{\rm HT} = -1.14 \pm 0.11$ with a χ^2 of 18.2 for 22 degrees of freedom. With $\lambda_{\rm DY}$ fixed at $\lambda_{\rm DY} = 1.0$, the fit gives $\lambda_{\rm HT} = -1.02 \pm 0.10$ with a χ^2 of 22.4 for 23 degrees of freedom. For $\lambda_{\rm DY}$ fixed at $\lambda_{\rm DY} = 1.0$ and $\lambda_{\rm HT}$ fixed at $\lambda_{\rm HT} = -1.0$, the fit gives χ^2 of 22.5 for 24 degrees of freedom. Thus, the Drell-Yan model with generalized higher twist provides a consistent picture of the angular distribution as well.

Since the model fits the data for $d\sigma/d\cos\theta$ rather well, it is natural to try to extract the α and β parameters (in the higher-twist part of the pion structure function) using these data rather than the $d^2\sigma/dx_\pi\,dx_N$ data. Taking $\lambda_{\rm DY} = 1.0$ and $\lambda_{\rm HT} = -1.0$, the expression for λ becomes

$$\lambda = \frac{F_0(x_\pi) - 2Ax_\pi^\alpha/m_{\mu\mu}^\beta}{F_0(x_\pi) + 2Ax_\pi^\alpha/m_{\mu\mu}^\beta}$$

at both naive and leading-log orders, where $F_0(x_\pi)$ is the lowest-twist piece of the pion structure function. The nucleon structure function drops out of this expression entirely (a result of the vanishing contribution of the pion sea at high x_π). At leading-log order $F_0(x_\pi)$ acquires the usual dependence on $m_{\mu\mu}$ through the Altarelli-Parisi equations. So, if $F_0(x_\pi)$ is known, one can estimate the higher-twist parameters A, α, and β by fitting to the measured values of λ shown in Fig. 13.

We took $F_0(x_\pi)$ from the fit over region A at leading-log order (no higher twist) with the results shown in Table IV. Because of a large correlation between α and β in these fits, it is not possible to let both α and β float simultaneously. While these fits strongly favor $\beta = 4.0$ over $\beta = 2.0$ (4σ statistical preference), there is a lack of statistical power to pin down the parameters.

VIII. CONCLUSIONS

In a new analysis of our data on the reaction $\pi^- N \to \mu^+\mu^- X$ at 253 GeV/c that includes muon pairs of mass as low as 3 GeV/c^2 we find improved evidence for higher-twist effects.

Drell-Yan models of $d^2\sigma/dx_\pi\,dx_N$ account for the bulk of the cross section, including that in the 3–4-GeV/c^2 mass region which is studied here for the first time. However, an extra term in the model is necessary to account for the increased cross section observed at low mass and high x_π (a 16-σ effect); this is true even when QCD corrections at the leading-log and next-to-leading-log order are included. Such a cross-section enhancement is predicted by Berger and Brodsky's higher-twist model [5, 15]. However, the data suggest (with 7-σ statistical significance) a $1/m_{\mu\mu}^4$ rather than $1/m_{\mu\mu}^2$ mass dependence for the higher-twist term in the pion structure function.

QCD corrections to the naive Drell-Yan model at leading-log and next-to-leading-log order improve the quality of the fits to the data slightly, and do not change the conclusions regarding the size of the higher-twist effects. However, the shape of the extracted nucleon function $G(x_N)$ changes significantly when QCD corrections are added: $G(x_N)$ is then more consistent with the parametrizations of Morfin and Tung [16], which are based on analysis of deeply inelastic scattering experiments. For $x_N < 0.06$ our nucleon structure function rises above that inferred from the analysis of Morfin and Tung, due to our sea-quark distribution being slightly larger than theirs in this region. Because of the model

TABLE IV. Results of fits to the form of $\lambda(x_N, x_\pi)$, where $d\sigma/d\cos\theta \propto 1 + \lambda\cos^2\theta$, in terms of parameters α and β of the generalized higher-twist contribution to the pion structure function.

α	β	χ^2	$N_{\rm DF}$	Probability
2.3 ± 1.3	2 (fixed)	36.9	22	0.02
2.9 ± 1.4	4 (fixed)	21.4	22	0.50
2 (fixed)	6.4 ± 1.4	17.1	22	0.76

dependence (i.e., lack of a QCD analysis to all orders, lack of leading-log evolution of the higher-twist effects, etc.) in determining the sea-quark distribution at low x_N from presently available data, this difference may not be significant.

The angular distribution $d\sigma/d\cos\theta$ approaches $1 - \cos^2\theta$ at low mass and high x_π, as predicted by Berger and Brodsky's higher-twist model [5]. For the lowest-mass data considered here ($m_{\mu\mu} \approx 3.0$ GeV/c^2), this higher-twist region extends down to $x_\pi \simeq 0.7$. Away from this region, we observed that $d\sigma/d\cos\theta \propto 1+\cos^2\theta$, as expected in the Drell-Yan model at lowest twist. The variation of the shape of the angular distribution over x_π-x_N space is more consistent with a higher-twist effect proportional to $1/m^4_{\mu\mu}$ than $1/m^2_{\mu\mu}$.

ACKNOWLEDGMENTS

We are pleased to acknowledge the dedicated work of the technical support groups both at our home institutions and at the Fermi National Accelerator Laboratory where the data were obtained. This work was supported by the U.S. Department of Energy under Contracts Nos. DE-AC02-76ER03072 and W-7405-ENG-82-KA0101 and by the National Science Foundation, Grant No. 83-03203.

APPENDIX A: PARAMETRIZATIONS AND SUM RULES FOR NUCLEON PARTON DISTRIBUTIONS

In using the full first-order-α_S QCD cross section to fit for pion and nucleon structure functions it was important to have parametrized forms for the nucleon parton distributions that could satisfy various constraints of experimental and theoretical origin. To minimize the computer time required to fit for the free parameters, it was also advantageous to require that the distributions be linear in the parameters: since both the Altarelli-Parisi evolution equations [11] and the first-order-α_S expressions [3, 4] are linear in the parton distributions, the predicted cross section is then also linear in the parameters.

The theoretical constraints applied to the nucleon parton distributions were the number and momentum sum rules

$$\int_0^1 \frac{u(x)}{x}dx = 2, \qquad \int_0^1 \frac{d(x)}{x}dx = 1,$$

$$\int_0^1 u(x)dx + \int_0^1 d(x)dx + 5\int_0^1 S(x)dx + \int_0^1 g(x)dx = 1,$$

where the coefficient 5 is based on analysis of deeply inelastic lepton scattering experiments [21] which show that the strange sea can be taken as $\sim \frac{1}{2}$ the up or down sea (and that the latter two distributions are identical). Here, u, d, S, and g refer to the u-valence-quark, d-valence-quark, u- or d-sea-quark, and gluon distributions in the proton, respectively. The Altarelli-Parisi evolution equations preserve these sum rules, so they may be applied at any value of Q^2.

From our 253-GeV/c π^- data set alone, it is not possible to differentiate between sea and valence quarks or between u and d quarks in the nucleon. Our procedure was to relate all nucleon parton distributions to a functional form for $u(x)$ via three additional constraints deduced from experiment. These constraints were

$$\frac{S(x)}{u(x)+d(x)} = 0.120(1-x)^{7.5}x^{-0.5},$$

$$\frac{d(x)}{u(x)} = 0.57(1-x),$$

$$\frac{g(x)}{u(x)+d(x)} = 1.20(1-x)^4x^{-0.5}.$$

The first of these is our measurement of the sea-to-valence ratio for nucleons in tungsten [22]. The second is from neutrino scattering measurements [21]. The third is based on the Duke-Owens [17] parametrization of the parton distributions. These constraints were applied at $Q^2 = (5.16\,\text{GeV})^2$, a value in the middle of the Q^2 range of the data.

The form chosen for $u(x)$ was

$$u(x) = \sum_{n=1}^{N} A_n \frac{x^{n-0.5}(1-x)^3}{B(n-0.5,4)},$$

where $N = 10$, $B(s,t) = \Gamma(s)\Gamma(t)/\Gamma(s+t)$ is the beta function, and A_n are the ten parameters to be determined by fitting to the data.

The sum rules provide three constraints on the parameters in $u(x)$. The number sum rules result in the two relations

$$2 = \sum_{n=1}^{N} A_n, \qquad 1 = 0.57\sum_{n=1}^{N} A_n \frac{8}{2n+7}.$$

The u integral in the momentum sum rule is given by

$$\int_0^1 u(x)dx = \sum_{n=1}^{N} A_n \frac{2n-1}{2n+7} = 2 - 1/0.57.$$

The experimental constraints on d, S, and g compared to u then lead to

$$\int_0^1 d(x)dx = 0.57\sum_{n=1}^{N} A_n \frac{8(2n-1)}{(2n+7)(2n+9)},$$

$$\int_0^1 S(x)dx = 0.12\sum_{n=1}^{N} A_n \left(1 + 0.57\frac{11.5}{n+11.5}\right)\frac{B(n,11.5)}{B(n-0.5,4)},$$

$$\int_0^1 g(x)dx = 1.2\sum_{n=1}^{N} A_n \left(1 + 0.57\frac{8}{n+8}\right)\frac{B(n,8)}{B(n-0.5,4)},$$

for the remaining integrals in the momentum sum rule.

Because the data from our experiment do not extend above $x_N = 0.34$, the sum rules cannot be applied immediately. It was necessary to constrain $u(x_N)$ to some reasonable value at high x_N; without this constraint the quark-distribution fit produced wild fluctuations for $x_N > 0.6$. The value of $u(x_N)$ for $x_N > 0.34$ actually has an influence on $u(x_N)$ for $x_N < 0.34$ through the sum rules imposed on the nucleon distributions, but this influence was not enough to force reasonable behavior for $u(x_N)$ at high x_N. The constraint used was based on the measurements of the proton structure function by Badier *et al.* [23] using 400-GeV/c protons: our $u(x_N)$ was required to be within ~ 0.003 of their measured $u(x_N)$ for $x_N > 0.65$. Their measured $u(x_N)$ is less than ~ 0.05 in this region; the influence on $u(x_N)$ for $x_N < 0.34$ due to the sum rules is consequently kept quite small.

After applying the sum rules, seven free parameters remained in the parametrizations of the nucleon parton distributions. In the non-naive formulations these parametrizations only provide starting values for the evolution of the parton distributions from a particular Q^2, taken here to be $(5.16\ \text{GeV})^2$.

APPENDIX B: NAIVE PARAMETRIZATION OF $d^2\sigma/dx_\pi dx_N$

In the naive Drell-Yan model the cross section may be written as

$$\frac{d^2\sigma}{dx_\pi\, dx_N} = (6.09\times 10^{-2}\ \text{nb/nucleon})\frac{F(x_\pi)G(x_N)}{(x_\pi x_N)^2}.$$

The constant factor above is just $4\pi\alpha^2/9s$ where $s = 475.2\ \text{GeV}^2$ for our experiment. The nucleon structure function $G(x_N)$ is subject to the normalization of the nucleon quark distributions described in Appendix A. The overall normalization is embedded in the pion structure function $F(x_\pi)$, which is allowed to vary without constraint to provide the best fit to the data.

The pion structure function is parametrized as

$$F(x_\pi) = \sqrt{x_\pi}(1-x_\pi)\sum_{i=0}^{5} A_i T_i\left(\frac{x_\pi - 0.7}{0.3}\right) + A_6\frac{x_\pi^{A_7}}{(m_{\mu\mu}/\sqrt{s})^{A_8}}.$$

The Chebyshev polynomials are defined by $T_n(y) \equiv \cos(n \arccos y)$. As the T_n are defined on the interval $[-1,1]$ but our data cover only $0.4 < x_\pi < 1$, we write the argument y of the $T_n(y)$ as $y = (x_\pi - 0.7)/0.3$. The parameters A_i are numerical constants and not functions of kinematic variables.

Parameters A_6–A_8 indicate the possibility of a higher-twist term in the pion structure function. In the Berger-Brodsky model [5, 15] parameters A_7 and A_8 are each fixed at a value of 2, while in our generalized higher-twist model they are free.

As described in Sec. VI A above, the nucleon structure function can be written as

TABLE V. Constants A_i and B_i for the parametrization of $d^2\sigma/dx_\pi\, dx_N$ given in Appendix B.

i	A_i	B_i
0	0.9508	1.9945
1	−0.3733	−0.4451
2	−0.2190	−0.3353
3	−0.0707	0.4687
4	−0.0978	0.6545
5	−0.0334	0.2223
6	2.84×10^{-5}	0.1255
7	3.046	0.2285
8	4.416	0.2773
9		0.1501

$$G(x_N) = \frac{x_N}{9}\left[4(0.5+\epsilon)u(x_N) + 4(0.5-\epsilon)d(x_N) + 5S(x_N)\right]$$

with $\epsilon = Z/A - \frac{1}{2}$. The $d(x_N)$ and $S(x_N)$ are derived from the parametrization of $u(x_N)$ as described in Appendix A.

As an example of the use of the naive parametrization, we report in Table V the numerical values of the A_i from fit 16 to the cross-section data over region B of Fig. 3. The resulting form for $F(x_\pi)$ is shown in Fig. 9. The corresponding results for the proton u-quark distribution are also reported in Table V as the coefficients B_i of the parametrization

$$u(x_N) = \frac{(1-x_N)^3}{\sqrt{x_N}}\sum_{i=0}^{9} B_i T_i(2x_N - 1),$$

where the argument of the Chebyshev polynomials follows from the restriction that $0 < x_N < 1$. The parameters B_i were obtained by reexpressing in a Chebyshev series the power-series form for $u(x_N)$ given in Appendix A, once the parameters of the power-series form had been determined from the fit to $d^2\sigma/dx_\pi\, dx_N$.

APPENDIX C: SOLVING THE ALTARELLI-PARISI EQUATIONS

This appendix documents the numerical method used to solve the Altarelli-Parisi equations [11] that determine the $Q^2(= m_{\mu\mu}^2)$ evolution of both the nucleon and pion parton distributions. As the initial condition, one specifies the parton distribution as a function of x at some value of Q^2; the parton distribution at arbitrary Q^2 is then obtained by solving the appropriate Altarelli-Parisi equation. Evolution equations of first order in α_S were used in this analysis.

The method will be illustrated for the valence distributions; the sea and gluon cases are similar. It is convenient to define $t = \ln(Q^2/\Lambda^2)$, where Λ is the QCD scale parameter ($\Lambda = 0.2$ GeV in this analysis). The strong running coupling α_S is then given by

$$\frac{1}{\alpha_S(t)} = \frac{33-2N_f}{12\pi}t$$

in the first-order scheme, where N_f is the number of flavors (we used $N_f = 4$). The evolution of the valence-quark distribution $p(x,t) = x[q(x,t) - \bar{q}(x,t)]$ is given by

$$\frac{dp(x,t)}{dt} = \frac{2\alpha_S(t)}{3\pi}\int_x^1 \frac{(1+z^2)p(x/z,t) - 2p(x,t)}{1-z}dz + \frac{\alpha_S(t)}{\pi}\left(1 + \frac{4\ln(1-x)}{3}\right)p(x,t).$$

Using the expression for α_S, this can be rewritten as

$$\frac{dp(x,t)}{dt}t = \mathcal{F}[p(x,t)],$$

where the linear functional $\mathcal{F}$ is given by

$$\mathcal{F}[p(x,t)] = \frac{\frac{8}{33-2N_f}\int_x^1 (1+z^2)p(x/z,t) - 2p(x,t)}{1-z}dz + \frac{12}{33-2N_f}\left(1 + \frac{4\ln(1-x)}{3}\right)p(x,t).$$

For each value of x, it is required only that $p(x,t)$ be known for all larger values of x; this allows us to leave the pion distributions unspecified for $0.0 < x < 0.4$.

By taking successive derivatives (while reversing the order of differentiation and integration), one can show that

$$t\frac{d^{n+1}p}{dt^{n+1}} = \mathcal{F}\left[\frac{d^n p}{dt^n}\right] - n\frac{d^n p}{dt^n}$$

for all $n \geq 0$. So, given $p(x,t_0)$, one can compute $d^n p(x,t_0)/dt^n$ for arbitrary n. To calculate $p(x,t)$ the Taylor expansion

$$p(x,t) = \sum_{n=0}^{N} \frac{d^n p(x,t_0)}{dt^n}\frac{(t-t_0)^n}{n!}$$

was used for some suitably high value of N. In practice, series of Chebyshev polynomials $T_m(x)$ were used to approximate the $d^n p(x,t_0)/dt^n$ for each n; the result was stored as the set of constants $A_{m,n}$ that appear in the expression

$$p(x,t) = \sum A_{m,n} T_m(x)(t-t_0)^n.$$

The range of m and n was $0 \leq n \leq 12$ and $1 \leq m \leq 32$, so over 400 constants $A_{m,n}$ were associated with each solution of the Altarelli-Parisi equations.

Several checks were performed to confirm that the implementation of the above algorithm provided an adequate solution to the Altarelli-Parisi equations. The first of these was to evolve a test function from $p(x,t_0)$ to $p(x,t_1)$, then apply the mechanism again to evolve $p(x,t_1)$ back to $p(x,t_0)$. The fact that the final $p(x,t_0)$ agreed with the initial test function to about 5 decimal places indicated that the implementation consistently evolved the distributions for both increasing and decreasing Q^2. The Altarelli-Parisi equations preserve the sum rules given in Appendix A. A second test was performed that verified that the sum rules were adequately satisfied over the desired Q^2 range. A third check compared the Duke-Owens [17] Q^2-dependent parametrizations with a distribution evolved as above from an initial Duke-Owens distribution. Here the calculated evolution agreed with the Duke-Owens forms to within the error specified for the Duke-Owens parametrizations.

APPENDIX D: FITTING AT NEXT-TO-LEADING-LOG ORDER

This appendix summarizes the method used for fitting for pion and nucleon structure functions via the so-called next-to-leading-log cross section $d^2\sigma/dQ^2\,dx_F$ of Kubar *et al.* [4] that includes all diagrams that are first order in α_S along with corrections to these evaluated to leading-log order in Q^2/Λ^2.

Given an hypothesis for the parton distribution functions for the pion and nucleon at a fixed reference value of Q^2 [$Q^2 = (5.16\ \text{GeV})^2$ was selected], the evolution equations were used to obtain the distribution functions at arbitrary Q^2 (as described above). Then the equations from Kubar *et al.* were used to calculate the expected cross section for $\pi^- N \to \mu^+\mu^- X$ at a given value of x_π and x_N. The calculated cross section was combined with the experimentally measured cross section and error to produce a contribution to χ^2, and the χ^2 was summed over bins in the x_π-x_N plane. By varying the input distribution functions to minimize χ^2 the optimum distribution functions were obtained.

The procedure for fitting at leading-log order was similar, except that the theoretical cross section did not include the Compton and annihilation graphs discussed below.

Because the computation of the cross section at a particular value of x_π and x_N involved integration over the intervals $[x_\pi, 1]$ and $[x_N, 1]$, values for the nucleon parton distributions were needed at high x_N (where we had no data). For this we used results from other experiments that studied high x_N, as discussed in Appendix A.

The QCD first-order α_S cross section is written as

$$\frac{d^2\sigma^i}{dQ^2\,dx_F} = \int dt_\pi\, dt_N\, \frac{d^2\hat{\sigma}^i(t_\pi,t_N)}{dQ^2\,dx_F} Q^i(t_\pi,t_N)\ ,$$

where t_π and t_N are the fractions of hadron momenta taken by the quark or gluon, and the index i = DY, A, or C labels the (naive) Drell-Yan, annihilation, or Compton components. $Q(t_\pi,t_N)$ is the joint distribution of quarks (or gluons) in the colliding hadrons.

For the Drell-Yan component,

$$\frac{d^2\hat{\sigma}^{\text{DY}}}{dQ^2\,dx_F} = \frac{4\pi\alpha^2}{9Q^2 s}\frac{\delta(t_\pi - x_\pi)\delta(t_N - x_N)}{x_\pi + x_N}.$$

The annihilation term is given by

$$\frac{d^2\hat{\sigma}^A}{dQ^2\,dx_F} = \tfrac{1}{2}A\frac{\delta(t_\pi - x_\pi)\delta(t_N - x_N)}{x_\pi + x_N}\left(1 + \tfrac{5}{3}\pi^2 - \tfrac{3}{2}\ln\frac{x_\pi x_N}{(1-x_\pi)(1-x_N)} + 2\ln\frac{x_\pi}{1-x_\pi}\ln\frac{x_N}{1-x_N}\right)$$
$$+\tfrac{1}{2}A\frac{\delta(t_N - x_N)}{x_\pi + x_N}\left(\frac{t_\pi^2 + x_\pi^2}{t_\pi^2(t_\pi - x_\pi)_+}\ln\frac{(x_\pi + x_N)(1-x_N)}{x_N(t_\pi + x_N)} + \frac{3}{2(t_\pi - x_\pi)_+} - \frac{2}{t_\pi} - \frac{3x_\pi}{t_\pi^2}\right)$$
$$+(\pi \leftrightarrow N) + \tfrac{1}{2}A\left(\frac{\tilde{G}^A(t_\pi, t_N)}{[(t_\pi - x_\pi)(t_N - x_N)]_+} + \tilde{H}^A(t_\pi, t_N)\right),$$

with

$$\tilde{G}^A(t_\pi, t_N) = \frac{(t_\pi + t_N)[\tau^2 + (t_\pi t_N)^2]}{(t_\pi t_N)^2(t_\pi + x_N)(t_N + x_\pi)}, \qquad \tilde{H}^A(t_\pi, t_N) = \frac{-2}{t_\pi t_N(t_\pi + t_N)}.$$

Here $\tau = x_\pi x_N$, and the distributions $1/(t-x)_+$, $1/[(t_\pi - x_\pi)(t_N - x_N)]_+$ are defined by

$$\int_x^1 dt\,\frac{f(t)}{(t-x)_+} = \int_x^1 dt\,\frac{f(t) - f(x)}{t - x},$$

$$\int_{x_\pi}^1 dt_\pi \int_{x_N}^1 dt_N\,\frac{f(t_\pi, t_N)}{[(t_\pi - x_\pi)(t_N - x_N)]_+} = \int\int dt_\pi\,dt_N\,\frac{f(t_\pi, t_N) - f(t_\pi, x_N) - f(x_\pi, t_N) + f(x_\pi, x_N)}{(t_\pi - x_\pi)(t_N - x_N)}.$$

The product of structure functions $Q(t_\pi, t_N)$ is

$$Q(t_\pi, t_N) = q(t_\pi, Q^2)\bar{q}(t_N, Q^2) + \bar{q}(t_\pi, Q^2)q(t_N, Q^2)\ ,$$

where q and $\bar{q}$ are Q^2-dependent quark and antiquark distributions (defined to be those measured in deeply inelastic scattering). The constant A is given by

$$A = \sum_q \frac{16\alpha^2\alpha_S(Q^2)e_q^2}{27Q^2 s},$$

where e_q is the quark charge in units of the proton charge.

The Compton term is given by

$$\frac{d^2\hat{\sigma}^C}{dQ^2\,dx_F} = \tfrac{3}{16}A\frac{\delta(t_N - x_N)}{(x_\pi + x_N)t_\pi^3}\left([x_\pi^2 + (t_\pi - x_\pi)^2]\ln\frac{(x_\pi + x_N)(1-x_N)}{x_N(t_\pi + x_N)} - 6x_\pi(t_\pi - x_\pi) + t_\pi^2\right)$$
$$+\tfrac{3}{16}A\left(\frac{\tilde{G}^C(t_\pi, t_N)}{(t_N - x_N)_+} + \tilde{H}^C(t_\pi, t_N)\right),$$

with

$$\tilde{G}^C(t_\pi, t_N) = \frac{\tau^2 + (t_\pi t_N - \tau)^2}{t_\pi^3 t_N{}^2(t_N + x_\pi)}, \quad \tilde{H}^C(t_\pi, t_N) = \frac{t_\pi(t_N + x_\pi)(t_N - x_\pi) + 2\tau(t_\pi + t_N)}{(t_\pi t_N)^2(t_\pi + t_N)^2}.$$

Here, $Q(t_\pi, t_N)$ is given by

$$Q(t_\pi, t_N) = g(t_\pi, Q^2)[q(t_N, Q^2) + \bar{q}(t_N, Q^2)]\ ,$$

where $g(t_\pi, Q^2)$ is the gluon distribution of the pion. The expression for $d^2\sigma^C/dQ^2\,dx_F$ is then

$$\frac{d^2\sigma^C}{dQ^2\,dx_F} = \int dt_\pi\,dt_N\,\frac{d^2\hat{\sigma}^C(t_\pi, t_N)}{dQ^2\,dx_F}Q^i(t_\pi, t_N) + (\pi \leftrightarrow N).$$

The main contribution to the cross section comes from the Drell-Yan and annihilation terms (roughly equal in size); the Compton terms are relatively small in size and negative. Since the parton distributions from deeply inelastic scattering calculated up to first order in α_S are defined to be the quark and antiquark distributions used above, the distributions should satisfy the (first-order) Altarelli-Parisi equations, as described in Appendix C. In fitting our data, the contribution of the heavy quarks is assumed to be negligible.

APPENDIX E: PARAMETRIZATION OF NEXT-TO-LEADING-LOG DISTRIBUTIONS AND K FUNCTION

This appendix presents parametrizations of the pion and nucleon distributions derived from fit 21 over region C at next-to-leading-log order including the generalized higher-twist term. Our analyses of parton distributions at

TABLE VI. Values used for $m_{\mu\mu}$-dependent parametrization of pion and nucleon structure functions given in Appendix E.

Parameter	$F_0(x_\pi)$ (lowest twist)	$u(x_N)$	$d(x_N)$	$s(x_N)$
α_0	2.3678×10^{0}	3.5046×10^{-1}	3.5258×10^{-1}	-2.7580×10^{-1}
α_1	-2.4142×10^{-1}	-2.4459×10^{-2}	-2.5166×10^{-2}	2.5422×10^{-2}
α_2	1.0175×10^{-3}	2.8217×10^{-3}	1.4586×10^{-3}	1.8067×10^{-4}
β_0	1.8034×10^{0}	5.2551×10^{0}	6.2622×10^{0}	8.9123×10^{0}
β_1	8.4144×10^{-2}	1.0205×10^{-1}	1.0784×10^{-1}	1.9644×10^{-1}
β_2	-1.2015×10^{-2}	-1.5418×10^{-2}	-2.0354×10^{-2}	-9.1696×10^{-2}
A_{00}	7.8242×10^{0}	1.5542×10^{1}	8.9186×10^{0}	-9.5118×10^{-2}
A_{01}	-1.2557×10^{0}	-1.9089×10^{0}	-1.1917×10^{0}	2.0474×10^{-2}
A_{02}	5.0750×10^{-2}	1.6236×10^{-1}	7.8515×10^{-2}	-6.5070×10^{-3}
A_{10}	-3.1864×10^{0}	1.8545×10^{1}	1.0645×10^{1}	-3.9667×10^{-1}
A_{11}	9.5306×10^{-1}	-2.5647×10^{0}	-1.5785×10^{0}	1.2185×10^{-2}
A_{12}	-1.0901×10^{-1}	2.2460×10^{-1}	1.1026×10^{-1}	-4.3150×10^{-3}
A_{20}	2.8832×10^{0}	4.0289×10^{0}	2.3170×10^{0}	-1.9703×10^{-1}
A_{21}	-6.3763×10^{-1}	-7.3296×10^{-1}	-4.3448×10^{-1}	1.2495×10^{-2}
A_{22}	3.4949×10^{-2}	7.4003×10^{-2}	3.5126×10^{-2}	4.3459×10^{-3}

leading-log and next-to-leading-log order did not utilize an explicit parametrization of their Q^2 dependence (unlike our previous work [10]). It may be convenient for the reader to have the results of our numerical integration of the Altarelli-Parisi equations parametrized as below.

Table VI contains the parameters associated with the pion and nucleon structure functions. The functional form used for $F_0(x_\pi)$, $u(x_N)$, $d(x_N)$, and $s(x_N)$ is

$$x^{\alpha_0+\alpha_1\tilde{t}+\alpha_2\tilde{t}^2}(1-x)^{\beta_0+\beta_1\tilde{t}+\beta_2\tilde{t}^2}\sum_{\substack{0\le i\le 2\\ 0\le j\le 2}} A_{ij}T_i(\tilde{x})\tilde{t}^j \ .$$

Here $\tilde{t} = \ln(m_{\mu\mu}^2/\Lambda^2) - 6.5$, $\Lambda = 0.2$ GeV. For the pion case, $x = x_\pi$, $\tilde{x} = (10x_\pi - 7)/3$. For the nucleon cases, $x = x_N$, $\tilde{x} = 2x_N - 1$. $F_0(x_\pi)$ is the lowest-twist term in the pion structure function. The parametrization of the cross section is then given by

$$\frac{d^2\sigma}{dx_\pi\, dx_N} = \frac{4\pi\alpha^2}{9s}\frac{G(x_N)}{(x_\pi x_N)^2}\left[K(x_\pi, x_N)F_0(x_\pi) + Ax_\pi^\alpha/(m_{\mu\mu}/\sqrt{s})^\beta\right] .$$

The K function $K(x_\pi, x_N)$ is calculated using the equations of Kubar *et al.* [4], as described in Appendix D. In this parametrization, $A = 2.40 \times 10^{-5}$, $\alpha = 2.834$, and $\beta = 4.448$.

The parametrization of the K function associated with these parton distributions is given by

$$K(x_\pi, x_N) = K_3 + (K_4\hat{x}_N + K_5\hat{x}_N^2 + K_6\hat{x}_N^3)\left[\hat{x}_\pi + K_7\hat{x}_\pi^2 + K_8\hat{x}_\pi^3 - K_9(x_N + K_{10})^{K_{11}}\right] ,$$

where $\hat{x}_\pi = x_\pi - K_1$ and $\hat{x}_N = x_N - K_2$. The 11 parameters K_i are given in Table VII.

Note that our parametrization of the pion structure function F_0 is restricted to the interval $0.4 < x_\pi < 1$, for which we have data.

TABLE VII. Values used for the parametrization of the K function given in Appendix E.

Parameter	Value
K_1	7.5333×10^{-1}
K_2	9.9794×10^{-2}
K_3	1.4844×10^{0}
K_4	2.3255×10^{0}
K_5	-7.7470×10^{0}
K_6	1.3933×10^{1}
K_7	4.8631×10^{0}
K_8	1.3329×10^{1}
K_9	-3.0208×10^{0}
K_{10}	-3.6483×10^{-3}
K_{11}	-6.2715×10^{-1}

APPENDIX F: $\psi'(3685)$ PRODUCTION

A study of J/ψ production in the present data sample has already been published [24]. To obtain an accurate continuum signal in the mass range 3–4 GeV/c^2, we have had to improve the resonance subtraction procedure compared to that of Ref. [24], and consequently can now present results for ψ' production as well.

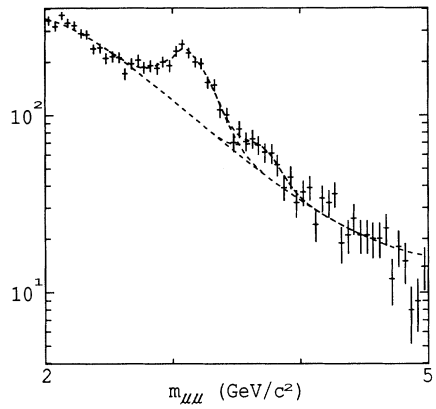

FIG. 14. Raw mass spectrum for $0.95 < x_F < 1$ used in ψ' analysis. The dashed curves are fits to the J/ψ, ψ', and continuum components.

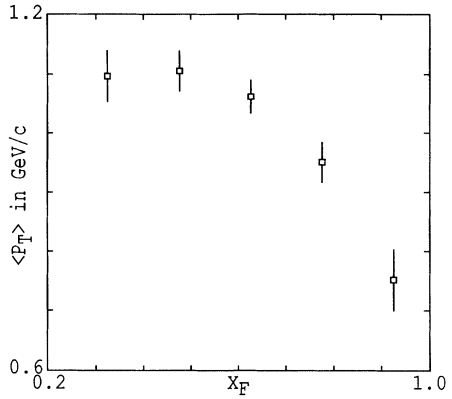

FIG. 16. The average p_T for ψ' production as a function of x_F.

As the resonances are produced predominantly by gluon-gluon scattering, the ratio of resonance to Drell-Yan continuum increases as x_F (or x_π) decreases. While the continuum signal is difficult to extract for $x_\pi < 0.4$, the resonance signals are rather reliable down to momenta such that the decay muons no longer penetrate to the rear of the detector, namely $x_F \sim 0.25$. Note that for a narrow resonance, x_π is a unique function of x_F, and we use the latter variable when discussing resonance production, following the custom in the literature.

Figure 14 shows the data and fitted resonance and continuum mass spectra for $0.95 < x_F < 1$. While the ratio of resonance to continuum is low in this region, the ψ' resonance is still quite distinct; the cross-section ratio $\sigma(\psi')/\sigma(J/\psi)$ discussed below is well determined even at large x_F.

The resonance subtraction leaves us with some 30 000 ψ' events with $x_F > 0.25$. We performed three cross-section analyses on these events: $d\sigma/d\cos\theta$, $d^2\sigma/dx_F\,dp_T^2$, and $d\sigma/dx_F$. These cross sections have been normalized to the result of Ref. [24] for $J/\psi \rightarrow \mu^+\mu^-$ production and decay that $B\sigma(x_F > 0.25) = 3.8$ nb/nucleon. In this, the dependence of the cross section on the atomic mass number A of the target has been taken to be $A^{1.0}$. The dependence of J/ψ production by pions has been reported [25] as $A^{0.87\pm0.02}$. If this value is also appropriate for ψ' production, the cross sections reported here should be multiplied by 2.0.

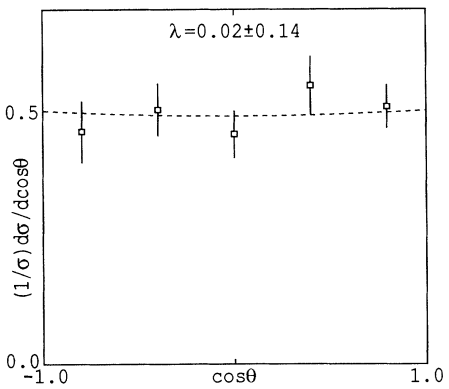

FIG. 15. The cross section $(1/\sigma)d\sigma/d\cos\theta$ for ψ' production. Also shown is a fit of the form $d\sigma/d\cos\theta \propto 1 + \lambda\cos^2\theta$ with $\lambda = 0.02 \pm 0.14$.

The angular dependence of the cross section for ψ' production with $x_F > 0.25$ is shown in Fig. 15. Characterizing this as

$$d\sigma/d\cos\theta \propto 1 + \lambda\cos^2\theta,$$

we find that $\lambda = 0.02 \pm 0.14$ with χ^2 of 2.0 for 3 degrees of freedom. While the variation of parameter λ with x_F might be indicative of the nature of the ψ' production mechanism, particularly at large x_F where higher-twist effects could contribute, our data sample was too small to yield statistically significant results for $\lambda(x_F)$.

The transverse-momentum dependence of ψ' production was studied via the cross section $d^2\sigma/dx_F\,dp_T^2$ for five bins of $x_F > 0.25$ and six bins of $p_T < 5$ GeV/c. These results were fitted to the empirical form (also used in Refs. [24] and [26] for the J/ψ)

$$d^2\sigma/dx_F\,dp_T^2 \propto (1 - x_F)^A/(1 + p_T^B/S)^T,$$

where $S = C + D(1 - x_F)^2$ and $T = E + F(1 - x_F)^2$.

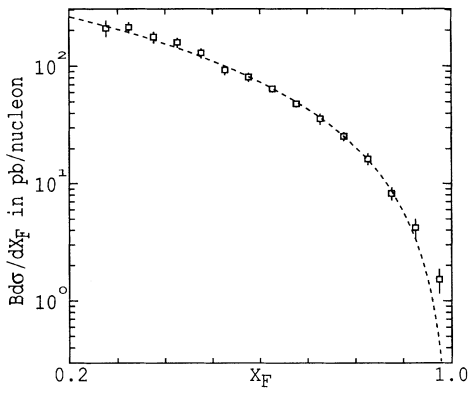

FIG. 17. The cross section $Bd\sigma/dx_F$ for ψ' production.

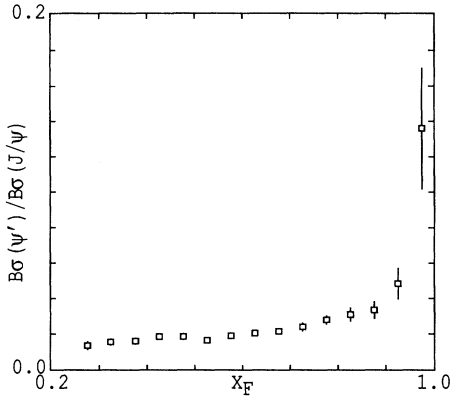

FIG. 18. Ratio of $Bd\sigma/dx_F$ for ψ' to J/ψ.

The results are

$$A = 1.35 \pm 0.03 ,$$

$$B = 1.67 \pm 0.02 ,$$

$$C = 2.5 \pm 0.2 ,$$

$$D = 114. \pm 2.0 ,$$

$$E = 7.3 \pm 0.2 ,$$

$$F = 84. \pm 2.0 ,$$

$$\chi^2/N_{\mathrm{DF}} = 32/23.$$

Perhaps the most interesting feature of this cross section is the dependence of the average transverse momentum on x_F, as shown in Fig. 16. The decrease in $\langle p_T \rangle$ at large x_F is seen in the production of all reasonably high-mass states [10, 24], and may indicate the decreasing importance of radiative gluon corrections at high x [26].

To provide greater detail in the dependence of ψ' production on x_F, we also measured the cross section $d\sigma/dx_F$ in fifteen bins of $x_F > 0.25$, as shown in Fig. 17. When we fit this to

$$d\sigma/dx_F \propto (1 - x_F)^A,$$

we find $A = 1.83 \pm 0.06$ with a χ^2 of 12 for 13 degrees of freedom. The highest-x_F data point lies significantly above the fit, and indicates that a single power-law fit is inadequate.

TABLE VIII. The cross section times branching ratio per nucleon as a function of x_F for J/ψ and ψ' production.

x_F	$d\sigma(J/\psi)/dx_F$ (pb/nucleon)	$d\sigma(\psi')/dx_F$ (pb/nucleon)
0.275	15 410±814	208±34
0.325	13 550±437	213±23
0.375	11 150±381	177±20
0.425	8653±246	159±16
0.475	7020±189	128±12
0.525	5535±123	92.7±8.4
0.575	4265±101	80.5±7.2
0.625	3167±74	64.5±4.1
0.675	2220±50	48.0±3.1
0.725	1475±41	35.7±3.8
0.775	922±27	25.6±2.2
0.825	522±16	16.1±1.9
0.875	246±11	8.3±1.1
0.925	87.6±5.0	4.2±0.8
0.975	11.2±0.9	1.5±0.4

A related quantity of interest is the ratio of the cross section for ψ' production to that for J/ψ production as a function of x_F, shown in Fig. 18. The cross sections for J/ψ and ψ' production (both measured in this experiment) that were used in the ratio calculation are also given in Table VIII. The rise in the cross-section ratio as x_F approaches 1 follows the trend of the argument given in Ref. [24]. While production of the J/ψ and ψ' at moderate x_F is dominantly due to gluon-gluon scattering, at very large x_F a quark-antiquark annihilation mechanism is favored for pion beams because of the valence antiquark in the pion. A Breit-Wigner model of the $q\bar{q}$ annihilation suggests that the resulting cross-section ratio $\sigma(\psi')/\sigma(J/\psi)$ is larger at high x_F than for gluon-gluon production mechanisms. The results shown in Fig. 18 support this interpretation. In Ref. [24] we showed that the large-x_F production of the J/ψ by $q\bar{q}$ annihilation is likely associated with a higher-twist effect, which is consistent with the theme of the present work.

At moderate x_F the production of the ψ' by gluon-gluon fusion is conceptually simpler than that of the J/ψ, much of which is due to the decay of P-wave χ states. Hence the ψ' cross sections should be of use in measurements of the gluon structure of the pion and nucleon. A determination of the gluon structure function of the pion from our ψ' cross sections alone will require knowledge of the gluon structure of the nucleon.

* Present address: Istituto Nazionale di Fisica Nucleare, Sezione di Torino, Torino, Italy.
† Present address: Fonar Corp., Melville, New York 11747.
‡ Present address: Los Alamos National Laboratory, Los Alamos, New Mexico 87545.
§ Present address: Stanford Linear Accelerator Center, Stanford University, Stanford, California 94309.
** Present address: Cornell University, Ithaca, New York 14853.
†† Present address: CERN, CH-1211 Geneva 23, Switzerland.
‡‡ Present address: Ecole Polytechnique Federal Lausanne,

CH-1006 Lausanne, Switzerland.
[1] J. H. Christenson *et al.*, Phys. Rev. Lett. **25**, 1523 (1970).
[2] S. D. Drell and T. M. Yan, Phys. Rev. Lett. **25**, 316 (1970).
[3] G. Altarelli, R. K. Ellis, and G. Martinelli, Nucl. Phys. **B157**, 461 (1979).
[4] J. Kubar *et al.*, Nucl. Phys. **B175**, 251 (1980).
[5] E. L. Berger and S. J. Brodsky, Phys. Rev. Lett. **42**, 940 (1979); E. L. Berger, Z. Phys. C **4**, 289 (1980).
[6] D. J. Gross and S. B. Treiman, Phys. Rev. D **4**, 1059 (1971).
[7] C. B. Newman *et al.*, Phys. Rev. Lett. **42**, 951 (1979); C. B. Newman, Ph.D. thesis, University of Chicago, 1979.
[8] K. J. Anderson *et al.*, Phys. Rev. Lett. **43**, 1219 (1979).
[9] S. Palestini *et al.*, Phys. Rev. Lett. **55**, 2649 (1985); S. Palestini, Ph.D. thesis, Princeton University, 1984.
[10] J. S. Conway *et al.*, Phys. Rev. D **39**, 92 (1989); J. S. Conway, Ph.D. thesis, University of Chicago, 1987.
[11] G. Altarelli and G. Parisi, Nucl. Phys. **B126**, 298 (1977).
[12] K. T. McDonald, in *High p_T Physics and Higher Twists,* Proceedings, Paris, France, 1988, edited by M. Benayoun, M. Fontannaz, and J. L. Narjoux [Nucl. Phys. B (Proc. Suppl.) **7B**, 104 (1989)].
[13] J. Badier *et al.*, Z. Phys. C **18**, 281 (1983).
[14] C. Biino *et al.*, Nucl. Instrum. Methods Phys. Res., Sect. A **243**, 323 (1986).
[15] S. J. Brodsky, E. L. Berger, and G. P. Lepage, in *Proceedings of the Workshop on Drell-Yan Processes*, Batavia, Illinois, 1982 (Fermilab, Batavia, 1982), p. 187.
[16] J. G. Morfin and W.-K. Tung, Z. Phys. C (to be published).
[17] D. W. Duke and J. F. Owens, Phys. Rev. D **30**, 49 (1984).
[18] P. Chiappetta and M. Le Bellac, Z. Phys. C **32**, 521 (1986).
[19] J. Badier *et al.*, Z. Phys. C **11**, 195 (1981).
[20] M. Guanziroli *et al.*, Z. Phys. C **37**, 545 (1988).
[21] F. Eisele, Rep. Prog. Phys. **49**, 233 (1986).
[22] J. G. Heinrich *et al.*, Phys. Rev. Lett. **63**, 356 (1989); J. G. Heinrich, Ph.D. thesis, University of Chicago, 1988.
[23] J. Badier *et al.*, Z. Phys. C **26**, 489 (1985).
[24] C. Biino *et al.*, Phys. Rev. Lett. **58**, 2523 (1987).
[25] S. Katsanevas *et al.*, Phys. Rev. Lett. **60**, 2121 (1988).
[26] C. E. Adolphsen, Ph.D. thesis, University of Chicago, 1985.